



UNIVERSITÄT ZU LÜBECK
INSTITUTE OF MATHEMATICS
AND IMAGE COMPUTING

Optimization of Image Registration for Determination of Regional Ventilation from CT Scans of the Lungs

Optimierung der Bildregistrierung zur Berechnung der regionalen Ventilation anhand von CT-Scans der Lunge

Masterarbeit

verfasst am

Institute of Mathematics and Image Computing

im Rahmen des Studiengangs

Mathematik in Medizin und Lebenswissenschaften
der Universität zu Lübeck

vorgelegt von

Maren Faber

ausgegeben und betreut von

Prof. Dr. Jan Modersitzki

Die Arbeit ist im Rahmen der Teilnahme am Programm DigiStrucMed der Medizinischen Hochschule Hannover in Zusammenarbeit mit dem Fraunhofer MEVIS Institut Bremen entstanden.

Lübeck, den 10. August 2022

Eidesstattliche Erklärung

Ich erkläre hiermit an Eides statt, dass ich diese Arbeit selbständig verfasst und keine anderen als die angegebenen Quellen und Hilfsmittel benutzt habe.

A handwritten signature in black ink that reads "Maren Faber". The signature is written in a cursive style with a long, sweeping underline that extends to the right.

Maren Faber

Zusammenfassung

Irreversible Schäden der Lunge wie beispielsweise eine Lungenfibrose können durch viele verschiedene Krankheiten ausgelöst werden und anhand der verminderten Ventilation der Lunge festgestellt werden. Dabei liefern herkömmliche Methoden wie der Lungenfunktionstest keine Aussage über regionale Veränderungen des Lungengewebes, weshalb medizinische Bildgebungsverfahren eine große Rolle in der Diagnose solcher Krankheiten spielen.

Im Rahmen dieser Masterarbeit wurde die Optimierung eines Bildregistrierungsnetzwerkes zur Bestimmung von Referenzwerten der regionalen Ventilation anhand von Lungen-CT-Scans durchgeführt. Dabei dienten die Jacobi-Determinanten des resultierenden Deformationsfeldes als Vorhersage für die regionale Volumenänderung.

Ein Fehlermaß zur Bewertung der Bildregistrierung wurde eingeführt und verschiedene Ansätze wurden miteinander verglichen. Es konnte gezeigt werden dass die separate Registrierung des linken und rechten Lungenflügels, sowie die Verwendung von maskierten Bildern zu besseren Ergebnissen geführt hat als die Registrierung der originalen CT-Scans. Der krümmungsbasierte Regularisierer mit einem zusätzlichen Volumenkontrollterm lieferte eine Transformation, die der erwarteten Lungenbewegung am ehesten entspricht.

Abstract

Irreversible damage of the lungs like for example a lung fibrosis can be triggered by many different diseases and can be identified by a decrease in lung ventilation. Conventional methods such as the pulmonary function test do not provide information about regional changes in lung tissue, which is why medical imaging techniques play a major role in the diagnosis of such diseases.

Within the scope of this master thesis, the optimization of an image registration network for the determination of reference values of regional ventilation based on CT scans of the lungs was performed. Here, the Jacobian determinants of the resulting deformation field served as a prediction for the regional volume change.

I introduced an error measure for evaluating image registration and compared different approaches. It could be shown that the separate registration of the left and right lung, as well as the use of masked images, led to better results than the registration of the original CT scans. The curvature regularizer with an additional term for volume control provided the most reasonable transformation, which most closely matched the expected lung motion.

Acknowledgements

First, I want to thank my supervisor Jan Modersitzki for his support and good advice. I want to thank Hoen-oh Shin for giving me the opportunity to participate in this interdisciplinary research project and to gain insight in clinical processes. I also would like to thank Stefan Heldmann from the Fraunhofer Institute for Digital Medicine MEVIS for the nice introduction to MeVisLab and for helping me with technical issues and questions.

Last but not least, special thanks go out to my parents who supported me through everything and made my studies possible and my boyfriend for keeping me motivated until the end and reading through this thesis.

Contents

1	Introduction	1
1.1	Contribution and Structure of this Thesis	2
1.2	Related Work	2
1.3	Medical Background	2
1.4	Mathematical Model of Image Registration	5
1.5	Experiments	5
2	Image Registration and Inverse Problems	7
2.1	Mathematical Problem	7
2.2	Similarity of Reference and Deformed Template	9
2.3	Parametric and Nonparametric Image Registration	10
2.4	Inverse Problems and Regularization	11
2.5	Jacobian Determinant as an Indicator for Volume Change	13
2.6	Numerical Implementation	17
2.7	Hypotheses	19
3	Methods	21
3.1	Image Preprocessing	21
3.2	Experiments on Patient Data	22
3.3	Image Registration Network	22
4	Results	27
4.1	VNC vs. 8-bit images	27
4.2	Separated lung registration vs. whole lung registration	29
4.3	SSD vs. NGF	31
4.4	Comparison of different regularization approaches	33
5	Discussion and Conclusion	47
5.1	Discussion	47
5.2	Conclusion of the Research Goal	49
5.3	Outlook	50
	Bibliography	51

1

Introduction

In the past decade the digitalization of medical processes and the use of automated software solutions especially in the field of diagnosis has become more and more important. An early detection of disease can be life saving for a lot of patients and therefore the period of time in which the diagnosis is unknown should be as short as possible. For example the use of neural networks in medical image processing such as segmentation, object detection or classification results in a faster and more precise identification of disorders while physicians are relieved from work (Kermany et al., 2018).

This work is part of a research project led by Hoen-oh Shin from the institute of radiology at Hannover Medical School. A problem with diagnostic methods commonly used in the pulmonary field such as PFT (pulmonary function testing) is that they only provide global information regarding the ventilation of the lungs. To get more regional information of the lungs medical imaging techniques have to be considered. Additionally, abnormalities in the deformation of the lungs are especially hard to spot since images are taken at a specific time and do not reflect movement. Therefore, the objective is to use lung CT scans in total expiration and inspiration to determine reference values of regional ventilation of the lungs.

This thesis introduces a mathematical approach to detect disruptions in the movement of the lungs which allows an early intervention to prevent irreversible damage of lung tissue like for example fibrosis. Within the scope of this research project image registration will be used to predict the deformation of the lungs during inspiration and expiration. Finally, a deformation field will be calculated which provides information about the regional volume change in every voxel.

The research question whether the mathematical approach of image registration can be used for clinical diagnosis of lung diseases by predicting the regional volume change and if this is faster than the conventional method will not be answered within the scope of this thesis as this requires clinical studies.

Instead, I'm going to elaborate on the question, which image registration model is best suited for imaging-based diagnosis in pulmonology and if the resulting Jacobian determinants can be used as a reasonable surrogate for regional volume change.

1.1 Contribution and Structure of this Thesis

The main focus of this thesis is the optimization of the image registration of lung CT scans which will be used to determine reference values for regional ventilation of the lungs. For this purpose I will introduce an error measure to determine the quality of the different approaches I'm going to test regarding the research goal. The different approaches are going to be tested on a set of anonymized patient data.

The first chapter includes a short introduction to the medical background and the mathematical model of image registration. The theory behind the mathematical model, the stated hypothesis and their motivation can be found in chapter 2. In chapter 3 a more detailed description of the implemented registration network and the execution of the experiments on patient data is provided. Finally, the results can be found in chapter 4, the discussion of the results and a conclusion of this thesis in chapter 5.

1.2 Related Work

The research question is based on a few clinical studies that examined the potential of CT-based diagnosis in pneumology. In (Fuld et al., 2008) the authors compared CT-measured regional volume change to regional ventilation of the lungs of anesthetized, intubated and mechanically ventilated sheep. They could show that there is a strong correlation between the non-invasive CT-specific ventilation and the regional specific volume change. Another study on patients with idiopathic pulmonary fibrosis (Scharm et al., 2021) investigated whether regional ventilation obtained by non-linear image registration of virtual non-contrast images in inspiration and expiration can serve as early imaging markers for disease progression in patients with IPF. They could show that the regional ventilation correlated with a future change of lung function.

The idea behind the research project that this thesis is part of comes from Hoen-oh Shin, who participated in the study (Scharm et al., 2021). He had the idea of implementing an automated work flow for CT scanners using image registration as a non-invasive diagnosis tool (Shin, 2021).

Regarding the image registration of pulmonary images in inspiration and expiration the authors of (Ruhaak et al., 2017) introduced an algorithm for the registration of pulmonary CT scans. The algorithm was submitted to the EMPIRE10 challenge (Murphy et al., 2011), which is the most comprehensive public comparison study on pulmonary image registration world wide, where it ranked first, thereby improving the state of the art in accuracy by 15% (Ruhaak et al., 2017).

1.3 Medical Background

This section presents a short introduction to the morphology and characteristics of the lungs in order to explain the following medical problem addressed in this thesis.

The human lungs are separated into the right and left lung which is slightly smaller and

shaped differently because it shares space with the heart. Air gets inhaled through the conducting zone, which includes all respiratory structures outside of the lungs for example nose or trachea, and into the bronchi, bronchioles and finally alveoli where the gas exchange takes place. The process of breathing is also called ventilation. A pleural sack which contains two separate membranes (pleurae) with pleural fluid in between them encases each lung. This allows the membranes to slide over each other smoothly while breathing. The inner pleura also separates both lungs into lobes, where the right lung contains three and the left one two lobes.

There are many respiratory diseases that lead to chronic damage of the lung parenchyma such as emphysema or fibrosis. Emphysema describes large air-filled spaces that are caused by breaking down of the walls of alveoli and is a major characteristic of chronic obstructive pulmonary disease (COPD). A fibrosis characterizes the scarring of lung tissue over time and can also be a result of emphysema. Both include symptoms like coughing, shortness of breath, chestpain or a feeling of tightness. In the field of diagnostics there are only two common procedures besides a lung biopsy which pose different medical challenges stated in the following paragraph.

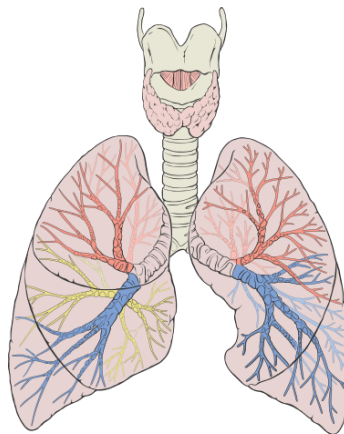


Figure 1.1: A diagram of the lungs showing the conducting zone, bronchi and bronchioles. Lobes are displayed in different colors. (Patrick J. Lynch, 2006)

Medical challenges in diagnosing pulmonary diseases

There are two types of methods commonly used to diagnose pulmonary diseases as mentioned previously. One of which is a pulmonary function test (PFT). For this non-invasive procedure the patient has to rapidly exhale into a sensory device called spirometer for as long as they can. This allows for detection of volume and speed of air that can be in- and exhaled. However, this method doesn't provide any information about regional ventilation. In the case of emphysema and fibrosis which in an early state are only detectable on a regional level, this information is essential for an early intervention. There is also some controversy about the forced exhaling of patients which can aggravate medical conditions and therefore is not always applicable (Clark, 2010).

Computed tomography (CT) is particularly relevant because changes in the lung paren-

chyma are not detectable with two-dimensional X-rays. CT scans provide a high-resolution three-dimensional image of the lungs which can be used for accurate evaluation of lung function and morphology. Despite high precision and the possibility of regional analysis of CT scans, patients are exposed to a relatively high amount of radiation. While an X-ray of the chest exposes the patient to approximately 0.1 mSv (millisievert) which is comparable with 10 days of natural background radiation, a CT scan of the chest leads to an effective radiation dose of 6.1 mSv. This equals a natural background exposure of 2 years (North America (RSNA) and Radiology (ACR), 2021). Therefore, the number of performed scans should be as low as possible to prevent cell damage which can lead to cancer. This limitation complicates the capturing of movement and deformation of the lungs while breathing. Typically, CT scans are performed on total inspiration and expiration. Additionally, the analysis of the images has to be done individually for every patient. This thesis presents an automated network to process lung CT scans, simulate the deformation of the lungs using image registration and compute a deformation field which will be used to calculate reference values for the regional ventilation. This will reduce expert workload and allows a faster diagnosis of lung diseases.

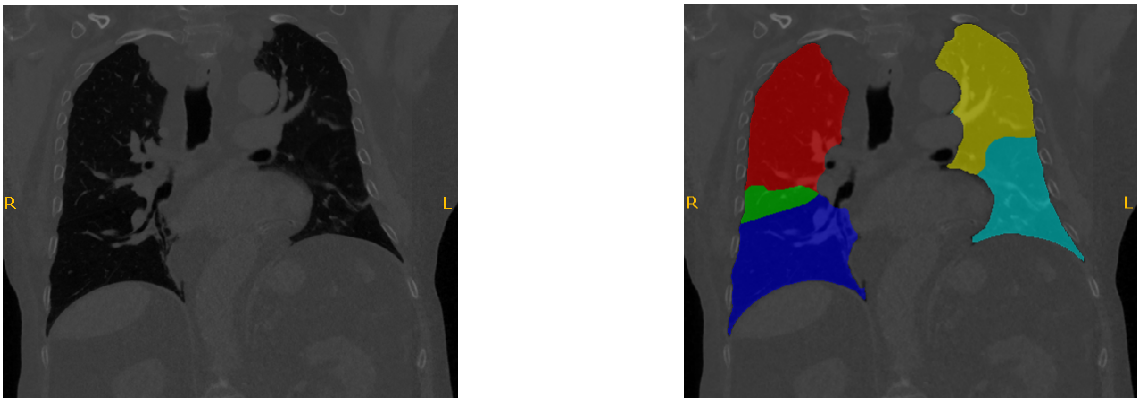


Figure 1.2: Left: Coronal CT scan of the lungs, Right: Coronal CT scan of the lungs with overlaid segmentation of lung lobes labeled with different colors. Further specifications can be find in chapter 3

Concept and Objective of the research project

As part of a research project this thesis focuses on the mathematical theory, optimization of the image registration and the implementation of the automated network. I'm going to give some more details about the project in this paragraph.

The main objective of this research is to use a large number of CT scans to calculate reference values for regional ventilation depending on the patient's age and sex. Physicians can use these reference tables to easily detect deviations from the norm. A visualization of pathological ventilation in form of a heat map could be an effective way to simplify the diagnosis of lung diseases. In a recent study on patients with idiopathic pulmonary fibrosis the researchers could show that an abnormally high regional ventilation can serve

as an early functional imaging marker for disease progression before the change of morphologic CT parameters or a decline in pulmonary function tests (Scharm et al., 2021). As CT scans cannot measure gas exchange of the lungs directly, fractional air volume change is used to represent lung ventilation (Shin, 2021), (Dettmer et al., 2018), (Scharm et al., 2021).

I will use an image registration approach to morphologically align CT images in inspiration and expiration. This will provide regional ventilation images in form of deformation fields. This automated image processing network will be used in a clinical study to compute the reference values for regional ventilation mentioned earlier in this section.

1.4 Mathematical Model of Image Registration

One of the biggest challenges in applied mathematics is to find a mathematical model that fits to the given problem. In this case the considered problem consists of a medical question in the field of radiology. As the problem calls for a model that computes a deformation from two images for this scenario CT scans of the lungs taken at different times an image registration model is the obvious choice. There is no unified image registration model that fits for every application field so in order to get reasonable solutions in an efficient way specifications of the basic image registration model are required (Modersitzki, 2009).

A basic image registration consists of two terms, the first one including some sort of distance measure and therefore indicating image similarity and the second one which is called regularizer measuring the plausibility or reasonability of the computed transformation. The focus of this thesis will be testing and comparing different settings for these two terms, variations of the input images and some parameter tuning in order to find a model that fits the given scenario the best. For the purpose of assessing the resulting transformations I'm going to define an error measure based on the Jacobian determinant which should be minimized by the model.

Further details on the mathematical model and the motivation behind the tested approaches and the use of the Jacobian determinant can be found in the next chapter. Additionally, I will elaborate on the numerics used in order to solve the optimization problem but since this is not the focus of this thesis I will keep this part as short as possible.

1.5 Experiments

To test the different approaches I'm going to perform experiments on anonymized patient data. Before registering the images, they are going to be preprocessed. After that I'm going to feed these images into the image registration network. Firstly, the images are going to be registered, then the deformation field will be computed. A visualization of the registration and the deformation fields help to visually check if the computation of the deformation provides a good alignment of the two images. The deformation fields will be saved for further computations and are going to be used in a clinical study in order to determine reference values on healthy patients. For analyzing the resulting transfor-

1 Introduction

mations I'm going to calculate mean values and variances of the Jacobian determinants to compare it with the quotient of volumina of the lungs in expiration and inspiration. The three different image data sets consist of the original lung CT scans, masked CT scans and last but not least masked scans separated into left and right lungs.

2

Image Registration and Inverse Problems

In image registration the main goal is to precisely align two or more images taken for example at different times or from different viewpoints. It is an important and often used tool to further analyze or compare medical images. Image registration is an inverse problem and therefore requires regularization (Fischer and Modersitzki, 2008). In this chapter I'm going to introduce a notation according to *FAIR: Flexible Algorithms for Image Registration* (Modersitzki, 2009) and further elaborate on the question why the registration problem is so difficult to solve.

2.1 Mathematical Problem

Before I'm going to give details on how such a registration model looks like I will specify some required notations that I will use throughout this thesis. Images are declared as functions as follows:

The reference image or fixed image $\mathcal{R} : \Omega_{\mathcal{R}} \subset \mathbb{R}^d \rightarrow \mathbb{R}$ and the template image also called moving image $\mathcal{T} : \Omega_{\mathcal{T}} \subset \mathbb{R}^d \rightarrow \mathbb{R}$ are both defined on compactly supported domains $\Omega_{\mathcal{T}, \mathcal{R}}$. d denotes the image dimension with $d = 2$ or $d = 3$ being the most common cases in medicine. For this thesis I will focus on $d = 3$ as the images used for the experiments are 3D scans of the lungs and the registration will also be done in 3D. $\mathcal{R} : \mathbb{R}^3 \mapsto \mathbb{R}$ will be the expirational and $\mathcal{T} : \mathbb{R}^3 \mapsto \mathbb{R}$ the inspirational image. These images map some point $x \in \Omega \subset \mathbb{R}^3$ of the image domain onto a scalar value which represents the grayscale value at a specific voxel of the image.

The choice of the lung CT scan in expiration as reference image is motivated by the medically reasonable outcome produced by this setting. Since the relaxed state of the lungs is in expiration and the process of breathing causes the lungs to expand we expect regional volume change values above 1 to imply expansion during ventilation. By choosing the inspirational image as reference the outcome would be between 0 and 1 which would imply shrinking.

With these notations we can now define a basic image registration model with the following objective function 2.1. Hereby, the goal is to find a transformation $y : \Omega_{\mathcal{R}} \rightarrow \mathbb{R}^3$ to map the template image \mathcal{T} onto the reference image \mathcal{R} so that the by y deformed template is similar to the reference.

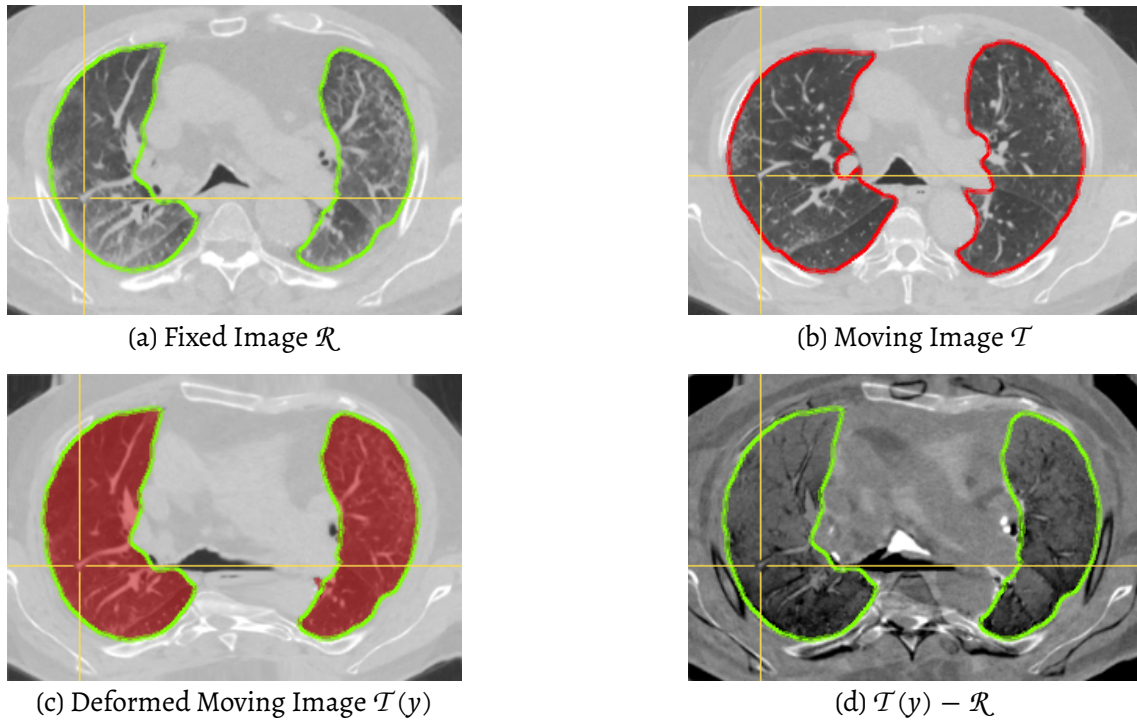


Figure 2.1: In axial view: (a) reference image in expiration with label in green, (b) template image in inspiration with label in red, (c) with y deformed template image in red in alignment with the label of the reference image in green, (d) difference of the deformed template image and reference image. Curser marks corresponding voxels in all four images, showing correct alignment of inner structures like blood vessels. Further details on the registration can be found in section 3.3.

Definition 2.1.

$$J(y) = \inf_y \mathcal{D}[\mathcal{T}(y), \mathcal{R}] \quad (2.1)$$

Where $\mathcal{T}(y) := \mathcal{T} \circ y : \Omega_{y(\mathcal{T})} \rightarrow \mathbb{R}$ describes the transformed template image with $\Omega_{y(\mathcal{T})}$ being the transformed image domain of the template and $\mathcal{D} : \Omega_{\mathcal{R}} \times \Omega_{\mathcal{T}(y)} \mapsto \mathbb{R}$ a distance measure in order to quantify similarity between $\mathcal{T}(y)$ and \mathcal{R} which will be specified in the next section 2.2. The functional $J(y) : y \mapsto \mathbb{R}$ maps the transformation y onto some scalar value. The goal is to minimize this value during the optimization process. Note that the objective function searches for an infimum rather than a minimum as the existence of a minimum can't be guaranteed. Figure 2.1 shows a registration example on lung CT scans. The difference of the deformed moving image and the reference image shows the similarity between the two images with small variances in the more detailed structures like blood vessels.

2.2 Similarity of Reference and Deformed Template

In this section I'm going to address different types of distance measures which represent similarity of the reference and deformed template image in the objective function $J(y)$. In order to compare $\mathcal{T}(y)$ and \mathcal{R} there are two different methods for detecting similarity of the images: feature-based or intensity-based.

For the first method, the so-called landmark-based registration, the similarity is measured by looking at specific points of the reference image, finding the corresponding points in the template image and calculating the distance between those corresponding points which then will be minimized in the optimization process. A huge drawback of this method is that the corresponding pairs of points, also called landmarks, have to be marked manually and the transformation is strongly dependent on the selection of landmarks. The resulting transformation can be easily adjusted by removing or adding landmarks but there are no rules on which combination of landmarks is the best. The choice of landmarks is also specific for every application scenario. Additionally, the resulting transformation is not physical, which means that there is no interaction between the individual landmarks and therefore there is no guarantee for a one-on-one transformation (Modersitzki, 2009). An example for landmark-based registration is the thin-plate-spline registration (Rohr, 2001).

As the choice of landmarks is challenging and often still requires manual intervention, intensity-based distance measures are a convenient alternative.

A common used intensity-based distance measure is the sum of squared differences (SSD) which is defined as follows:

Definition 2.2. Given the images $\mathcal{T}(y)$ and \mathcal{R} the SSD measure is

$$\mathcal{D}^{SSD}[\mathcal{T}(y), \mathcal{R}] := \frac{1}{2} \int_{\Omega} (\mathcal{T}(y(x)) - \mathcal{R}(x))^2 dx. \quad (2.2)$$

It measures the energy contained by the difference image and in order to be meaningful, it has to be assumed that the gray values of corresponding points are more or less the same in the reference and template images (Modersitzki, 2009).

In the case of the lungs the inflowing air causes a change in density of the lung tissue which leads to differences of several hundred Hounsfield units between corresponding structures (Castillo et al., 2013). The Hounsfield scale is frequently used in CT scans, describes radiodensity and can be interpreted as a measurement for the attenuation of x-rays by the tissue (Buzug, 2004). Since this characteristic of the lungs do not guarantee comparability of the grey values the requirements for SSD are not met so a different distance measure is required.

A distance measure that focuses on image edges rather than the absolute intensities is the normalized gradient field (NGF) distance measure. In the lungs edges are represented by the bronchial tree, blood vessels, the lung boundary and fissures and the alignment of such structures is desired. Therefore a variant of the NGF distance measure was introduced by (Ruhaak et al., 2017) for overcoming the problem of intensity change in lung CT scans.

The definition is given by:

Definition 2.3. For the images $\mathcal{T}(y)$ and \mathcal{R} the NGF distance measure is defined by

$$\mathcal{D}^{NGF}[\mathcal{R}, \mathcal{T}(y)] := \int_{\Omega_{\mathcal{R}}} 1 - \frac{\langle \nabla \mathcal{T}(y(x)), \nabla \mathcal{R}(x) \rangle_{\eta}^2}{\|\nabla \mathcal{T}(y(x))\|_{\eta}^2 \|\nabla \mathcal{R}(y)\|_{\eta}^2} dx \quad (2.3)$$

with $\langle f, g \rangle_{\eta} := \eta^2 + \sum_{j=1}^3 f_j g_j$ and $\|f\|_{\eta}^2 := \langle f, f \rangle_{\eta}$.

$\eta > 0$ being an edge parameter for suppressing noise-related edges.

This metric is defined to measure the alignment of the two gradient fields t of \mathcal{T} and r of \mathcal{R} and is zero (minimal) for $t = \pm r$ and 1 (maximal) if t is orthogonal to r or one of them is equal to 0. The authors of (Ruhaak et al., 2017) chose the NGF distance measure because of its efficient computation, robustness and suitability for numerical optimization.

Although there are more kinds of intensity-based distance measures available, in this thesis I'm going to compare SSD and NGF with regard to pulmonary image registration.

In the next section I'm going to describe the transformations used to deform the template images so they are as similar to the reference as possible and therefore minimizing the distance measure.

2.3 Parametric and Nonparametric Image Registration

In order to align the template and reference image there are different kinds of transformations commonly used in image registration. In this section I'm going to present some types of transformations, their features and purpose with regard to image registration. Primarily, the transformations used in image registration can be divided into affine-linear and non-linear or deformable transformations. Affine transformations are characterized by their line- and parallelism-preserving features and can be described as $y(x) = Ax + b$ for some point $x \in \Omega \subset \mathbb{R}^3$ with $A \in \mathbb{R}^{3 \times 3}$ being an invertible matrix and $b \in \mathbb{R}^3$ the translation vector. In this setting the wanted deformation function is defined as follows: $y : \mathbb{R}^3 \times \mathbb{R}^{3 \times 3} \times \mathbb{R}^3 \mapsto \mathbb{R}^3$. A very important subset of affine transformations are rigid transformations which additionally are length- and angle-preserving. They are also called Euclidean transformations because the Euclidean distance between every pair of points is being preserved and include rotations, reflections and translations. Although these transformations are very simple and quickly computed they only provide a rough alignment of the lungs as the complex movement of the lungs cannot be approximated by global affine transformations. For example since the lungs "hang" inside of the thorax and the ventilation process is mainly set in motion by the diaphragm at the bottom of the lungs the deformation in the lower half of the lungs is stronger than in the upper half. There are other features of the lungs like for example asymmetry or the texture of lung tissue that make the movement of the lungs very complex and therefore the image registration model requires nonlinear deformation for precise alignment in a local environment.

To further refine the registration we need deformable transformations which allow local deformation also called "warping" of the image. These can also be subdivided into parametric and nonparametric models. As the name suggests, parametric deformable transfor-

mations depend on a finite set of parameters (thus including affine transformations) and therefore result in a rather small system of equation which can be solved easily and with low computing time.

Nonparametric deformable transformations result in arbitrary mapping for each point of the image allowing for precise local alignment. However, nonparametric image registration can lead to extensive computation time as a highly underdetermined system of nonlinear equations has to be solved. Additionally, the nonparametric model is very likely to get stuck in local minima and thus requires a good starting point. These described features of parametric and nonparametric registration models lead to the obvious and efficient combination of both models: Parametric image registration is often used for preregistering the images in order to get a reasonable starting point for a nonparametric image registration. This approach results in low computation time as the high-costly nonparametric transformations are only used for small corrections of the transformation computed by the preregistration.

Since a nonparametric registration model leads to a highly underdetermined system of equations this high degree of freedom requires regularization. Before I give a few examples of often used types of regularizers I want to further describe the problem of ill-posedness of inverse problems.

2.4 Inverse Problems and Regularization

Image registration is one of the most complex optimization problems in image processing (Modersitzki, 2009) which is strongly related to the fact that it is an inverse problem. To give insight on the complexity of inverse problems let's first have a look at an example for a direct or so-called forward problem: The goal hereby is to find a point B on a map with given directions starting from point A. The solution for this problem is easy to find and unique to the given conditions.

The corresponding inverse problem or backward problem would be if point A and B are given, which way did the person go to get from A to B? Not are there only infinite ways to get from point A to B but there are also many solutions that we don't want to consider as they are impossible in a realistic scenario (for example flying over the buildings would be very fast but not possible).

Further requirements in order to get a reasonable solution like stopover points or finding the shortest connection between points A and B are essential. In image registration A and B are represented by the images we want to align and the goal is to find a transformation to map one image onto the other. Therefore image registration is a highly underdetermined and ill-posed inverse problem.

A mathematical problem is well-posed if the following properties first introduced by (Hadamard, 1902) apply:

Definition 2.4.

1. a solution exists
2. the solution is unique

3. the solution's behavior changes continuously with the initial conditions

These properties allow for a stable solving algorithm and prevent error amplifying. Otherwise the problem is considered to be ill-posed.

Typically, regularization is a way to include prior knowledge to set restrictions or further requirements like smoothness for the wanted function y . It is a helpful tool to ensure a unique solution for underdetermined ill-posed problems like nonparametric registration models. As stated before in section 2.1 the regularizer measures reasonability of the transformation and will now be added to the objective function 2.1 as the second term of our registration model:

$$J(y) = \inf_y \mathcal{D}[T(y), \mathcal{R}] + \alpha S(y) \quad (2.4)$$

with $\alpha > 0$. $S(y) : y \mapsto \mathbb{R}$ is a functional mapping from the function space of the transformation y to the space of real numbers.

An example for a regularizer commonly used in image registration is linear elastic regularization (Broit, 1981). In this method objects in the image are considered to be made of elastic material and the regularizer corresponds to the linear elastic potential caused by the deformation of the elastic material. As the linear elasticity model is blind to rigid transformations because its theory is based on relations of points, a preregistration is required (Modersitzki, 2009).

Other regularization approaches that are based on the second order derivatives are the curvature regularizer (Fischer and Modersitzki, 2003) and the gradient-based diffusive regularizer (Fischer and Modersitzki, 2002).

A more recent form of regularization introduced by (Burger, Modersitzki, and Ruthotto, 2013) is the hyperelastic regularizer. This method can handle especially large nonlinear deformations and guarantees diffeomorphic (bijective and continuously differentiable map with continuously differentiable inverse) transformations as the penalty for non-diffeomorphic transformations approaches infinity. This makes the hyperelastic regularization a useful method to prevent ill-posedness. The hyperelastic regularizer consists of three parts:

Definition 2.5.

$$S^{hyper}(y) := \int \alpha_1 length(y) + \alpha_2 surface(y) + \alpha_3 volume(y) dx \quad (2.5)$$

where $\alpha_i > 0$ are parameters for the three components length, surface and volume which correspond to the three invariants gradient, cofactor and determinant of the transformation.

This regularizer allows us to control change of length, surface and volume by weighing and defining individual penalty functions like follows:

Definition 2.6.

$$\begin{aligned}
 \text{length}(y) &= \Phi_\ell(\nabla y), & \Phi_\ell(X) &= \|X - I_d\|_{Fro}^2, \\
 \text{surface}(y) &= \Phi_{w,c}(\text{cof } \nabla y), & \Phi_w(X) &= (\|X\|_{Fro}^2 - 3)^2, \\
 & & \Phi_c(X) &= \max\{\|X\|_{Fro}^2 - 3, 0\}^2, \\
 \text{volume}(y) &= \Phi_v(\det \nabla y), & \Phi_v(x) &= ((x - 1)^2/x)^2,
 \end{aligned} \tag{2.6}$$

with Frobenius-Norm $\|X\|_{Fro} := \sqrt{\sum X_{ij}^2}$ and ∇y being the Jacobian matrix (see definition 2.8).

A detailed definition of the cofactor in this setting can be found in (Burger, Modersitzki, and Ruthotto, 2013) and a definition of the determinant in 2.5.

The penalty chosen for controlling changes in area is the double-well function Φ_w which is zero for no change in area and positive otherwise. Since the double-well function is not convex (Burger, Modersitzki, and Ruthotto, 2013) introduced the convex envelope Φ_c of Φ_w and presents an existence proof for this setting. Ideally, the objective function should be convex as standard arguments, like every local minimum of a convex optimization problem is also a global minimum, apply (Burger, Modersitzki, and Ruthotto, 2013)(Florian Jarre, 2004). A drawback of using the convex envelope as a penalty function is that it doesn't penalize surface shrinkage.

The volume penalty is chosen so that shrinkage and growth are equally priced.

It is further suggested by the authors to search for transformations in the Sobolev space $W^{1,2}(\Omega, \mathbb{R}^3)$ where cofactor and determinant are sufficiently integrable and the determinant is positive (Burger, Modersitzki, and Ruthotto, 2013).

Further details on the application of this concept for my experiments can be found in the next chapter.

In the next section I'm going to elaborate on the importance of the Jacobian determinant and introduce an error measure to determine the quality of the image registration in order to compare different approaches.

2.5 Jacobian Determinant as an Indicator for Volume Change

Regarding the research goal stated in the introduction, studies have shown that the ratio of lung volumina in inspiration and expiration can be used as a surrogate for lung ventilation and that CT-based regional ventilation has the potential to serve as an early imaging marker for various lung diseases (Fuld et al., 2008)(Solyanik et al., 2015)(Dettmer et al., 2018)(Scharm et al., 2021).

In this section I'm going to show why the Jacobian determinant is related to volume change and can further be used for the determination of reference values for regional lung ventilation as it indicates volume change in every voxel for reasonable deformations.

First, since it is a key element in this thesis I'm going to give a definition for volume.

Definition 2.7. For some given set A its volume is defined as

$$\text{vol}(A) = \int_A dx \tag{2.7}$$

for $x \in A$.

Note that the set used to determine lung volume is given by the binary lung mask provided by the automatic segmentation of the lungs (Winther et al., 2020).

Before I will discuss the relation between volume and the Jacobian determinant let's first have a look at the definitions of the Jacobian matrix and determinant.

As most optimization algorithms like Gauss-Newton (Bertsekas, 1995) are gradient-based processes the Jacobian matrix is used to compute first order partial derivatives. For a transformation $y : \Omega \subset \mathbb{R}^3 \rightarrow \mathbb{R}^3$ in a three-dimensional setting the Jacobian matrix in a point $z \in \Omega$ is defined as follows:

Definition 2.8.

$$\nabla y(z) = \left(\frac{\partial y_i}{\partial x_j}(z) \right)_{i,j=1,2,3} = \begin{pmatrix} \frac{\partial y_1}{\partial x_1}(z) & \frac{\partial y_1}{\partial x_2}(z) & \frac{\partial y_1}{\partial x_3}(z) \\ \frac{\partial y_2}{\partial x_1}(z) & \frac{\partial y_2}{\partial x_2}(z) & \frac{\partial y_2}{\partial x_3}(z) \\ \frac{\partial y_3}{\partial x_1}(z) & \frac{\partial y_3}{\partial x_2}(z) & \frac{\partial y_3}{\partial x_3}(z) \end{pmatrix} \quad (2.8)$$

with x_1, \dots, x_3 being the coordinates of a point x in the original image.

The Jacobian determinant so the determinant of the Jacobian matrix gives information about the behavior of the transformation y in each point and is defined by:

Definition 2.9.

$$\det \nabla y := \partial_1 y_1 \partial_2 y_2 \partial_3 y_3 + \partial_2 y_1 \partial_3 y_2 \partial_1 y_3 + \partial_3 y_1 \partial_1 y_2 \partial_2 y_3 - \partial_1 y_3 \partial_2 y_2 \partial_3 y_1 - \partial_2 y_3 \partial_3 y_2 \partial_1 y_1 - \partial_3 y_3 \partial_1 y_2 \partial_2 y_1 \quad (2.9)$$

with $\partial_i y_j = \frac{\partial y_j}{\partial x_i}$ for $i, j = 1, 2, 3$.

Now back to the research question and to why we can use the Jacobian determinants of the deformation field as a prediction for local volume change. This correlation shows the theorem for integration by substitution for higher dimensions (Forster, 2012).

Theorem 2.10. *Let $\Omega \subseteq \mathbb{R}^d$ be an open set and $y : \Omega \rightarrow y(\Omega) \subseteq \mathbb{R}^d$ a diffeomorphism. Then a function f on $y(\Omega)$ is integrable when the function $x \mapsto f(y(x)) \cdot |\det(\nabla y(x))| dx$ is integrable on Ω . In this case the following condition applies:*

$$\int_{y(\Omega)} f(z) dz = \int_{\Omega} f(y(x)) \cdot |\det(\nabla y(x))| dx \quad (2.10)$$

with $\nabla y(x)$ being the Jacobian matrix and d spacial dimension.

A proof for this theorem can be found in (Forster, 2012). This especially shows that the volume of some object in the original setting on Ω and the volume of the transformed object on $y(\Omega)$ are connected by the Jacobian determinant. Note that the requirements for

theorem 2.10 are met because the hyperelastic regularizer 2.5 guarantees diffeomorphic transformations (Burger, Modersitzki, and Ruthotto, 2013). Further, if we consider the ratio of volumina it shows that:

$$\lim_{\epsilon \rightarrow 0} \frac{\text{vol}(y(\mathcal{B}(x_0, \epsilon)))}{\text{vol}(\mathcal{B}(x_0, \epsilon))} = |\det \nabla y(x_0)| = \begin{cases} > 1 & \text{volume expands;} \\ = 1 & \text{volume stays the same;} \\ < 1 & \text{volume shrinks.} \end{cases} \quad (2.11)$$

where $\mathcal{B}(x_0, \epsilon)$ is a sphere with center x_0 and radius ϵ .

In addition to this, the Jacobian determinant behaves in the same way as the ratio of volumes if we swap reference and template images. In detail this means that we receive the reciprocal value of the Jacobian determinant in some point by swapping the reference and template image. To show this correlation, let's have a look at the forward and backward mapping of an image registration.

First, if we apply a forward mapping y and backward mapping y^{-1} on some point $x \in \Omega$ we receive the identity function which maps x onto itself. This gives us the following relation:

$$I = \nabla Id(x) = \nabla[y(y^{-1}(x))] = \nabla y(y^{-1}(x)) \cdot \nabla y^{-1}(x) \quad (2.12)$$

where ∇ is the partial derivative or Jacobian, Id the identity function and I the identity matrix. In the last step the chain rule was applied. The next step will be to apply the determinant to equation 2.12 which gives us the following statement:

$$1 = \det(I) = \det[\nabla y(y^{-1}(x)) \cdot \nabla y^{-1}(x)] = \det[\nabla y(y^{-1}(x))] \cdot \det[\nabla y^{-1}(x)] \quad (2.13)$$

Under the condition that the determinants are unequal to 0 we can divide by $\det[\nabla y(y^{-1}(x))]$ and get:

$$\det[\nabla y^{-1}(x)] = \frac{1}{\det[\nabla y(y^{-1}(x))]} \quad (2.14)$$

Of course as $\det[\nabla y(x)]$ corresponds to the Jacobian determinant we showed that the Jacobian determinant of the backward mapping is equal to the reciprocal value of the Jacobian determinant of the forward mapping.

For the last step we assumed that the determinants are unequal to 0 which is fulfilled by diffeomorphic transformations. This can be derived from a corollary of the implicit function theorem (Forster, 2012):

Corollary 2.11. *Let $U \subseteq \mathbb{R}^d$ be an open set and $f : U \rightarrow \mathbb{R}^d$ a continuously differentiable map. Let $a \in U$, $b := f(a)$ and the Jacobian matrix $\nabla f(a)$ be invertible. Then there are open neighborhoods $U_a \subseteq U$ of a and V_b of b , so that f maps the set U_a bijectively onto V_b and the inverse function $g = f^{-1} : V_b \rightarrow U_a$ is continuously differentiable or in short: $f|_{U_a}$ is a diffeomorphism.*

Since the Jacobian matrix is a quadratic matrix it is invertible if the determinant is unequal to 0.

This property was used in (Burger, Modersitzki, and Ruthotto, 2013) to show that the resulting deformation is diffeomorphic as all Jacobian determinants were unequal to 0.

In conclusion, a positive determinant means that the orientation stays the same (no inversion), determinants greater than 1 can be interpreted as expansion and values between 0 and 1 as shrinkage caused by the transformation y . Negative determinants, as well as determinants close to 0 and very large determinants are not to be expected for the lung registration model. As the reference image is the expirational image the Jacobian determinants are expected to be similar to the ratio of volumina of template and reference, which in most cases should be a value between 1 and 3.

For the following experiments this implies that a registration of pulmonary CT scans in expiration and inspiration is considered to be good if the difference of the volume ratio and the expected value of the Jacobian determinants of the resulting deformation field is minimal, respectively goes to zero.

This leads to the following definition of an error measure for the transformation

$$y : \Omega_{\mathcal{R}} \rightarrow \mathbb{R}^3:$$

Definition 2.12. For given template and reference images \mathcal{T} and \mathcal{R} the registration error is

$$error(y) := \left\| \frac{vol(\mathcal{T})}{vol(\mathcal{R})} - \overline{\nabla y} \right\|_2 \rightarrow 0 \quad (2.15)$$

with $\overline{\nabla y} := \frac{1}{n} \sum_i \nabla y(x_i)$ and $x_i \in y(\Omega_{\mathcal{R}})$ for $i = 1, \dots, n$ being the expected or mean value of the Jacobian determinants and $\|\cdot\|_2$ being the Euclidean norm.

This measure will be used for analyzing different registration models tested in the experiments.

Before I'm going to formulate the hypotheses I want to further investigate within this thesis, I'm going to make a quick stopover to mention the numerics that are used in order to solve the optimization problem 2.4. Although the numerical implementation is not the focus of this thesis it is a big challenge in mathematics and therefore I want to elaborate on the numerics used for the experiments.

2.6 Numerical Implementation

The images and the optimization problem 2.4 are defined in a continuous setting as they are modeled in order to solve a medical problem which of course deals with continuous properties of objects. Additionally, many image transformations require a continuous image model since the transformed image does not align with a pixel grid (Modersitzki, 2009).

Of course the CT scans are voxel-wise measurements and therefore only available in a discrete setting. So in order to switch between discrete and continuous settings different kinds of discretization and interpolation schemes are needed.

In this section I'm going to elaborate on the types of numerics used within the scope of this thesis.

Discretize-then-Optimize

In order to solve a continuous problem there are two options on how to proceed. Either optimize-then-discretize, which means finding the continuous optimality conditions analytically and optimizing the resulting system of equations, or discretize-then-optimize so optimizing the discretized optimality conditions. In the case of image registration problems, they do not allow for an analytic solution (Modersitzki, 2009) and therefore the discretize-then-optimize approach is used to apply standard optimization algorithms.

To get the discretized objective function it has to be defined on a grid. There are different approaches to do so, for example evaluating the image in the centers of each cell of an overlaid grid, a so-called cell-centered grid. For detailed descriptions of the discretization process I'm referring to (Modersitzki, 2009).

In this setting the discretized objective function of 2.4 looks like this:

Definition 2.13.

$$J^h(y_c) = \inf_{y_c} \mathcal{D}^h[\mathcal{T}(y_c), \mathcal{R}(x_c)] + S^h(y_c - y_{Ref}) \quad (2.16)$$

where $y_c \approx y(x_c)$ is the current transformed grid, \mathcal{D}^h and S^h are the discretized distance measure and regularizer and y_{Ref} is a discrete reference for regularization for example $y_{Ref} = x_c$.

Note that a discretized representation of the hyperelastic regularizer can be found in (Burger, Modersitzki, and Ruthotto, 2013).

Discretizing the optimization problem also allows for a multilevel-registration approach where the problem is first solved on a coarse grid and the obtained solution will then be used as a starting point for the next finer level until the original resolution of the images is restored. On a coarse grid the optimization problem is relatively easy to solve and therefore it yields cheap computational costs. Another advantage is that by getting rid of the details and only keeping the main features of the images it prevents the optimization process from running into local minima. On the finer and more expensive levels only small corrections of the before computed approximations are required which additionally leads to lower computation time. As all discrete problems are linked by the same

continuous model the sequence of discrete solutions y^h approximates the solution of the continuous model (Modersitzki, 2009). As this approach reduces computation time it is applied within this thesis.

For solving the before stated discretized optimization problem 2.16 there are different types of Newton-based techniques available (Bertsekas, 1995). Regarding the Gauss-Newton algorithm the approximation of the Hessian matrix can get quite expensive and therefore the BFGS method is a good alternative as it estimates the Hessian on the fly (Modersitzki, 2009). From the family of quasi-Newton methods BFGS stands for Broyden-Fletcher-Goldfarb-Shanno and because it does not require an explicit computation of the inverse Hessian its computational complexity is only $O(n^2)$ compared to $O(n^3)$ for Newton-based methods (Jorge Nocedal, 2006). For optimization problems with many variables like image registration the approximative variant of the BFGS algorithm the limited-memory BFGS (ℓ -BFGS) is used to limit computer memory during computation. Since the ℓ -BFGS algorithm was already employed in related works dealing with pulmonary image registration like (Ruhaak et al., 2017) and considering its computation time reducing properties I'm going to apply this method likewise.

Image Interpolation

Like described above, CT scans are usually available in a discrete setting and in order to get a continuous representation of these images interpolation strategies are applied.

The most simple interpolation scheme would be the next neighbor interpolation (Thevenaz, Blu, and Unser, 2000) which basically is represented by the voxel-wise measurements of a CT scan where a value is assigned constantly to the whole voxel (cell). This approach is usually not applied in image registration as the derivative of the interpolant is either undefined or 0 which leads to problems in the optimization process (Modersitzki, 2009).

An intuitive approach for interpolating the image values is the linear interpolation. The values at the cell centers are connected by section-wise defined linear functions. This method can easily be adapted for 2D (bilinear) and 3D (trilinear) scenarios and ensures that the interpolated values don't exceed the span of measured values (no overshooting). A drawback of linear interpolation is that it is only almost everywhere continuous (Modersitzki, 2009).

A more complex approach is the spline interpolation where the goal is to get a smooth and continuous representation by finding a function interpolating the data and minimizing its bending energy (Modersitzki, 2009). This method originates in shipbuilding where wooden slats were bent around piles without snapping. The resulting cubic spline is very smooth but can lead to oscillatory behaviour and overshooting.

Of course there are other ways of interpolating data but with the goal of reducing computation time in order to process huge amounts of patient data at once these are probably the most efficient ones.

For my experiments I used the trilinear interpolation scheme as it enables matrix-free computations and therefore further reduces computation time. Matrix-free computation is a method where the matrices (for example gradient and Hessian) are not explicitly stored but are accessed through matrix-vector products. (Rühaak, 2017) discusses the ap-

plication of matrix-free techniques for efficient image registration.

Now, after elaborating on all challenges of setting up an image registration model I'm going to formulate some hypotheses I want to further investigate during the experiments which are going to be described and discussed in the following chapters.

2.7 Hypotheses

With optimizing the image registration being the goal of this thesis I'm going to test and compare different approaches regarding the minimization of the error measure defined in 2.12. Note that an image registration is considered to be more precise than another if the error value is smaller.

More details on the execution of the experiments can be found in the next chapter. The discussion of the results regarding the hypotheses can be found in chapter 5.

1) Separate Registration of left and right lung

For the first hypothesis the idea is to separately register the right and left lung. This approach can be directly derived from the morphology of the lungs. Since the left lung is differently shaped because it shares space with the heart and only consists of two lung lobes compared to the right lung which consists of three lung lobes (see figure 1.1) it is also expected that it moves differently than the right lung during the ventilation process. Therefore, the first hypothesis states that a separate registration, which can also mean a different set of parameters for each registration, of the right and left lung can lead to a more precise prediction of regional lung ventilation than registering the whole lung at once.

In order to test this hypothesis I'm going to use two sets of images where the first set consists of the original lung CT scans and the second set consists of two subsets being the separated left and right parts of the original images. Of course the corresponding segmentation masks also get separated into a left and right part. As the left and right lung are only connected by the trachea (which isn't a part of the lungs according to the labeling) overlapping of the left and right part is excluded which simplifies cutting the images.

2) Registration of masked lung CT scans

The second hypothesis is that registering the masked lung CT scans is more precise than registering the original scans. Masked in this case means that the lung labels are used to crop the images so only the region including the lung parenchyma remains. An example of the cropped images can be found in figure 3.1.

This approach comes from the idea of simulating the pleural sack which encases the lungs and restricts its movement at the boundary of the lungs. As described in the introduction the pleural sack contains of two membranes which slide along each other while breathing. By restricting the deformation to the lung region of interest the necessity of recovering this non-continuous sliding motion is removed and the remaining motion inside

of the lungs is considered to be very smooth (Ruhaak et al., 2017).

Additionally, the masked images are stored as 8-bit grayscale images which means the image values are between 0 and 255 (2^8 values in total) in order to save computer memory. Another advantage of using 8-bit images for the image registration is that the contrast of the inner structures is increased and therefore alignment of the edges should be more precise.

To test this hypothesis I'm going to compare two sets of images, the first one containing the original images and the second one the cropped 8-bit images.

Of course I'll test this approach in combination with the first hypothesis of separately registering the left and right lung, so there will also be masked versions of the separated images. In the following I'm going to refer to the original images as VNC images and to the masked images as 8-bit images as it matches the file names created during images preprocessing.

3) Hyperelastic Registration

The third hypothesis states that a hyperelastic regularization model yields a fast and precise image registration of lung CT scans and is therefore considered as a suitable and efficient regularizer for pulmonary image registration. To test its performance I'm going to compare it to the curvature and diffusive regularizer and show that the hyperelastic regularizer leads to a more precise image registration while having a comparably short computation time.

The parameters I'm going to investigate are the regularization weights α , respectively α_i for $i = 1, 2, 3$ of the hyperelastic regularizer.

Further details on the tested intervals of parameters can be found in section 4.4.

4) Normalized gradient field

The fourth hypothesis states that the NGF distance measure yields for a more precise image registration than SSD. Like discussed before in section 2.2 the NGF distance measure is more suited to pulmonary image registration as it does not depend on absolute intensities values. Additionally, the requirements for SSD are usually not met by lung CT scans which should lead to inaccurate results.

3

Methods

In this chapter I'm going to specify the experimental execution of the previously described approaches in order to answer the research question and investigate the above proposed hypotheses.

The CT scans I used within the scope of this thesis were performed at the Hannover Medical School for retrospective analysis of clinically acquired CT data at the fibrosis outpatient clinic of pneumology. These scans are three-dimensional VNC (virtual non-contrast) images of a patient's thorax in inspiration and expiration from a base and follow-up examination and are available in the DICOM format. DICOM which stands for *Digital Imaging and Communications in Medicine* is the international standard of medical images and related informations and is implemented in almost every medical imaging device (Horii and Bidgood, 1993). Additionally, a neural network (U-Net) automatically segmented the images in order to get corresponding labels of the lung region (Winther et al., 2020). As seen in figure 1.2 the five lung lobes are labeled in different colors. After preprocessing, the images and labels serve as the input of the registration network implemented in MeVisLab (Ritter et al., 2011). More details on the image registration network can be found in section 3.3.

3.1 Image Preprocessing

One objective of the research project of which this work is part of is to implement an automatic work flow which involves all preprocessing steps plus the image registration and evaluation. Since normally, the preprocessing has to be done by hand and individually for every patient an automated work flow for clinical use saves a lot of time and allows to process a huge amount of patient data.

As this thesis focuses on the image registration I'm going to briefly describe the preprocessing steps with an example and will not go into the work flow any further.

Image preprocessing was done using MATLAB ver. R2022a. Within the research project I received Matlab scripts written by Prof. Dr. Hoen-oh Shin which needed further adaptations. First, the labels that were originally created by an automated lung segmentation network (U-Net by (Winther et al., 2020)) needed some corrections as neural networks

don't guarantee a flawless segmentation of the pulmonary tissue. My contribution to the preprocessing was adding the deletion and correction of wrong labels to the existing Matlab script as well as applying all preprocessing steps on the provided patient data. Common errors of automated segmentation networks are labels that occur outside of the lungs, wrong labelling of lung tissue or shifting.

The next step was to mask the original CT images with the corresponding labels in order to test the second hypothesis.

The last step was to divide all images (including original VNC images and masked images) and label images into a left and right part to test the first hypothesis.

After preprocessing there are 6 sets of images in total including the corresponding label images: the original images, the cropped images, the original divided in left and right images and the cropped images divided in left and right. All images and labels are now available in the NifTI format. NifTI stands for *Neuroimaging Informatics Technology Initiative* and is used for data exchange.

Figure 3.1 shows an example containing all three preprocessing steps.

3.2 Experiments on Patient Data

The provided patient data I worked with were previously anonymized. It consists of data from 69 patients with images in total expiration and inspiration and corresponding labels from a base and follow-up examination. So 138 sets of inspirational and expirational images in total. Using python script modules I implemented an automated workflow for my experiments.

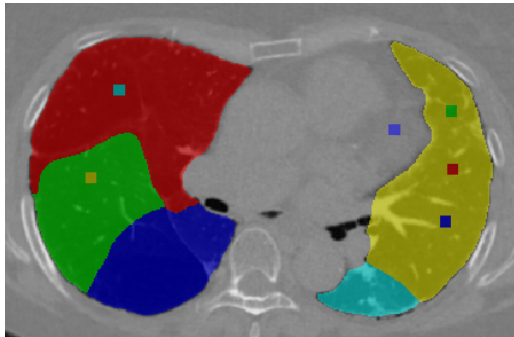
First, the images were automatically loaded and fed into the lung registration module. I used the label images to calculate the lung volume in expiration and inspiration in order to get the volume ratio. Furthermore, by using thresholds I created label images for the individual lung lobes which are labeled with numbers 1-5. This allowed me to additionally calculate the volume of the lung lobes which I used for a more regional analysis of the results. After the registration of the input images the Jacobians of the deformation field were computed (see next section).

In addition, I documented the run time of the registration (including preregistration and main registration).

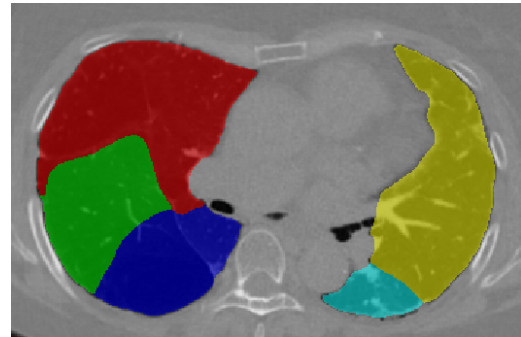
All computations will be included in a loop over all patient data.

3.3 Image Registration Network

After preprocessing the images serve as the input for the image registration network implemented in MeVisLab. MeVisLab is a framework for image processing with focus on medical imaging. It contains a wide range of software modules for segmentation, registration as well as functional analysis. For this thesis MeVisLab was chosen for the implementation because it is specialized for medical image processing and related works like (Ruhaak et al., 2017) and (Grob et al., 2019) already used it for pulmonary image registration.



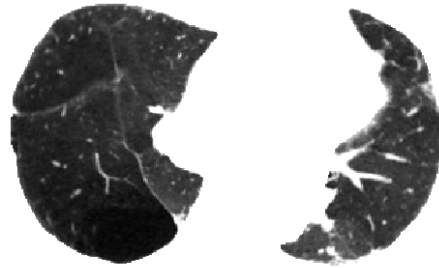
(a) Segmented lung lobes with manually added labeling errors



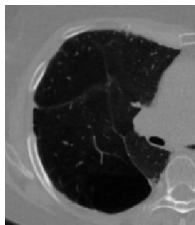
(b) Corrected segmentation



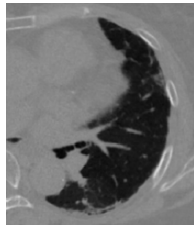
(c) Original VNC image



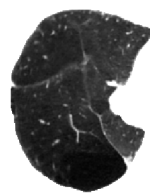
(d) Masked image



(e) Separated VNC image of the right lung



(f) Separated VNC image of the left lung



(g) Separated masked image of the right lung



(h) Separated masked image of the left lung

Figure 3.1: Example of the automated image preprocessing on patient data. The original CT scan was performed in total expiration at the fibrosis outpatient department of pneumology at the Medical School Hannover. All images are displayed in axial view. The rows represent the preprocessing steps 1-3 while the bottom two rows show an example of each of the 6 different image sets I will use in the experiments.

Networks implemented in MeVisLab resemble flowcharts where the individual modules (for example for image loading or processing) are connected to result in a data-flow. The direction of the data-flow goes from the bottom of the interface to the top so the input nodes are on the bottom of the modules and the output nodes on the top. There is also the possibility of grouping multiple modules to divide the network into subnetworks for a better overview. The created networks can be modified dynamically by Python scripts at runtime. In the following I'm going to describe the implemented network in detail and present a schematic representation in figure 3.2.

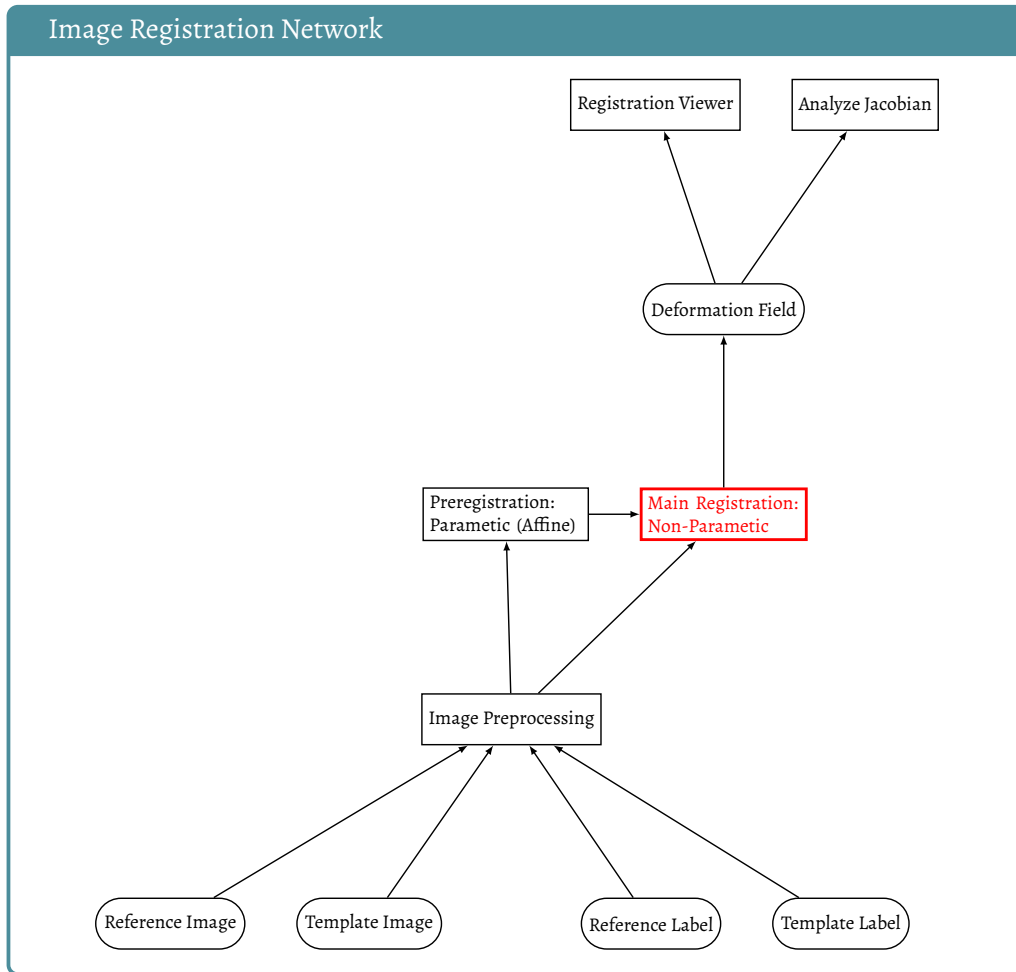


Figure 3.2: Schematic diagramm of the image registration network implemented in MeVisLab. Rectangles represent image processing steps while rounded rectangles represent input and output images of the network. The flow chart direction resembles the direction of data flow in the MeVisLab interface. The red box marks the main focus of this thesis.

The image registration network takes four images in the NifTI format as input which would be the fixed reference image in expiration, the moving template image in inspiration and the two corresponding label images. These were then fed into a lung registration module. This module is a so called macro module that contains a subnetwork of modules

itself. First step of the image registration is image preprocessing to prepare the input images for the registration modules. Image preprocessing includes scanning for minimum and maximum values of the images, cropping the images as well as extracting encoded image informations. These preprocessed images were then forwarded to two different image registration subnetworks.

Affine Preregistration

First, a preregistration using an affine registration module was performed in order to get an initial transformation estimation for the following main registration. The preregistration parameters will not be changed during experiments and they are given as follows: The distance measure used for the affine preregistration is the SSD distance measure, a multi-level approach using 3 levels (with the second finest level as end point) and Gaussian-downsampling was employed and for the optimization process the Gauss-Newton algorithm has been used. The resulting transformation will be forwarded to the main registration module and used as a starting point for the non-parametric registration.

Non-parametric Main Registration

The main registration consists of a nonparametric registration module which takes the preprocessed images and the transformation computed by the affine preregistration as inputs. This is where parameter tuning will be performed during the experiments. The motivation behind the choice of parameters and different approaches can be recalled in chapter 2.

First, I'm going to list the constant values that are not going to be changed during experiments:

The nonparametric registration is performed as a multi-level registration with five levels. As for the example registration in figure 2.1 the finest level and the original image size is $394 \times 264 \times 303$. For the next coarser level the image dimensions are halved (decimals are rounded down) which results in dimensions $12 \times 8 \times 9$ for the coarsest level. Obviously registration starts at the coarsest level and ends with the finest.

Like I mentioned in the chapter before, the interpolation scheme of choice is linear (trilinear for 3D images) interpolation.

The optimization algorithm chosen for the experiments is the ℓ -BFGS algorithm because of its fast computation features presented in 2.6. Additionally, matrix-free computations were employed in all registrations.

The variables that will be tested mainly involve the two terms of the optimization problem 2.4, the distance measure $\mathcal{D}[\mathcal{T}(y), \mathcal{R}]$ and the regularizer $\mathcal{S}(y)$.

For the distance measure I will compare the NGF with the SSD distance measure like described in the fourth hypothesis and the weight is constantly set to 1, therefore it doesn't appear in the equation.

For both the curvature and diffusive regularizer I'm going to test values for the regularizer weight α in the intervall $[0, 2.6]$ in steps of 0.2. An analysis of the choice of this intervall can be found in the next chapter.

According to the definition 2.5 the hyperelastic regularizer consists of 3 terms controlling length, surface and volume. The length term coincides with the diffusive regularizer, therefore the parameter α becomes α_1 for the hyperelastic approach. For the volume controlling term I chose the rational function as penalty function like defined in 2.6. Although there are other options for this function to test these would go beyond the scope of this thesis. For the weight α_3 I'm going to test values in the intervall $[0.001, 0.002]$ in steps of 0.00025.

Unfortunately, the surface controlling term is not implemented in MeVisLab, yet. Therefore the weight α_2 will simply get set to 0.

The example registration shown in figure 2.1 was performed on VNC images with the following configurations: Registration was done in 3D using matrix free computations. As distance measure normalized gradient fields (NGF) and for regularization the curvature regularizer with weighting $\alpha = 1$ were used. Finally, a linear interpolation scheme was chosen. Like described before, this registration was performed with a multi-level approach.

Deformation Field and Jacobians

The output of the lung registration is a deformation field which will be used to calculate the deformed template image but also for a further evaluation of the image registration. These deformation fields will get saved in the NifTI format.

In order to visualize and review the results, a registration viewer was used which similar to the example 2.1 displays the input images, the with the computed transformation deformed template image and the difference. There are other vizualisation options available in the registration viewer. The Jacobian was computed from the deformation field and displayed with another viewer. Also pictured in this viewer is a histogram of the Jacobians. Examples of the vizualisations can be found in the next chapter.

For the evaluation of the performed image registrations I used the output to calculate the mean (expected) value and variance of the Jacobians over the reference label (or the lung lobe labels for regional analysis like described in section 3.2). As mentioned before, the mean value of the Jacobians should be approximately the same as the volume ratio which is why I defined the error measure 2.12. A small variance of the Jacobians indicates a smooth transformation. These values are used to evaluate the registration and to compare different paramter settings.

All values including volumina, volume ratio, Jacobian mean and variance values as well as the computation time of the registration were saved in CSV files.

4

Results

In this chapter I'm going to present the results of the performed experiments considering the in section 2.7 established hypotheses. In order to compare the different registration approaches I will look at the evaluated error measure, the distributions of the Jacobians, and the output of the registration network itself.

First I'm going to investigate the hypotheses considering the input images (hypothesis 1 and 2) before I'm going to compare different parameters with the goal of optimizing the image registration.

All registration examples are from the same patient as in example 2.1 and displayed as a 2D slice in axial view.

4.1 VNC vs. 8-bit images

To test the second hypothesis that registering the masked 8-bit images is more precise than the original VNC scans I performed all computations with two sets of images. The first set including the VNC images and the second including the cropped and to 8-bit converted images. I calculated the mean error after definition 2.12 over all computations and additionally documented the mean Jacobian, the mean standard deviation (STD) and average runtime of the registration. The calculated values can be found in table 4.1. A box-plot of the error values can be found in figure 4.2

VNC original vs. 8-bit masked				
data set	error	volume ratio	Jacobian \pm STD	runtime in s
VNC	0.20691	1.82094	1.61617 \pm 0.43959	34.30
8-bit	0.11148	1.82094	1.81179 \pm 0.36260	34.25

Table 4.1: Comparison of the two data sets VNC and 8-bit. Note that the mean volume ratio is equal for both sets as all computations were performed using the same patient data.

Table 4.1 implies that using the cropped 8-bit images for image registration improves

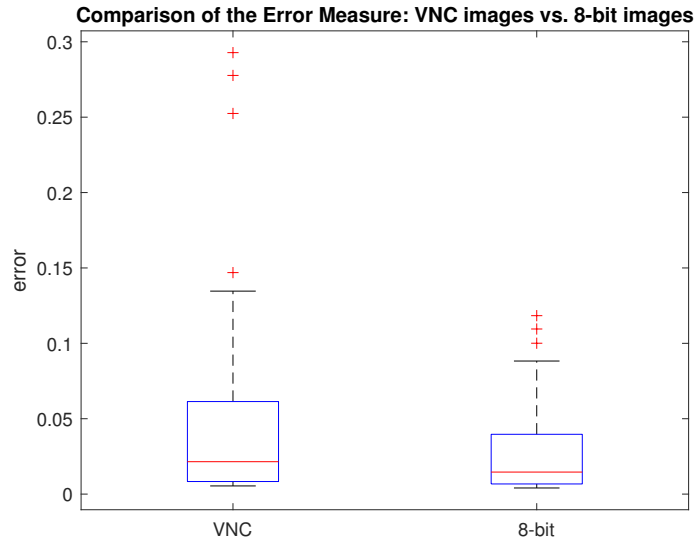


Figure 4.2: Boxplot of the error values over all experiments, comparing the two input data sets VNC and 8-bit. Note that the three outliers in data set VNC were computations using the SSD distance measure.

the error and the computed Jacobians yield for a better representation of the regional volume change. While the runtime seemed not to be affected the deviation of the Jacobians is smaller when registering the 8-bit images compared to the original VNC images, which implies a smoother deformation and corresponds with the error values.

A more detailed look at the error values gives the boxplot in figure 4.2. Overall, the boxplot for the 8-bit images is more compact showing the lower deviation. The minimum is at 0.004, maximum at 0.118 and the median at 0.015. For the VNC data set the minimum lies at 0.005, maximum at 0.293 and median at 0.021. Excluding the outliers, the maximum would be at 0.135 which still would be higher than the maximum for the 8-bit data set. The VNC outliers were caused by the computations using the SSD distance measure implying that SSD is not applicable for VNC data.

Although the medians of both sets aren't that far apart the registration with the 8-bit images seems to be way more stable leading to smaller deviations for all experiments and therefore smoother deformations.

In figure 4.3 a registration example is shown to compare the effect of the VNC and 8-bit input images on the outcome. The registration was done using the NGF distance measure and the curvature regularizer with α set to 1. Like described before, all experiments were done using a trilinear interpolation scheme and the ℓ -BFGS optimization algorithm.

Looking at the deformed template images in figure 4.3 both registrations fit the reference label well. There's only one part at the bottom half of the left lung (which is the lung on the right in the images) where the deformed template does not fit within the reference label which occurs for both VNC and 8-bit input images.

Regarding the difference images the main dissimilarity is that the difference image for the VNC images is higher in contrast especially at the outline of inner structures like along blood vessels, bronchial tubes or lung fissures. This implies a less precise align-

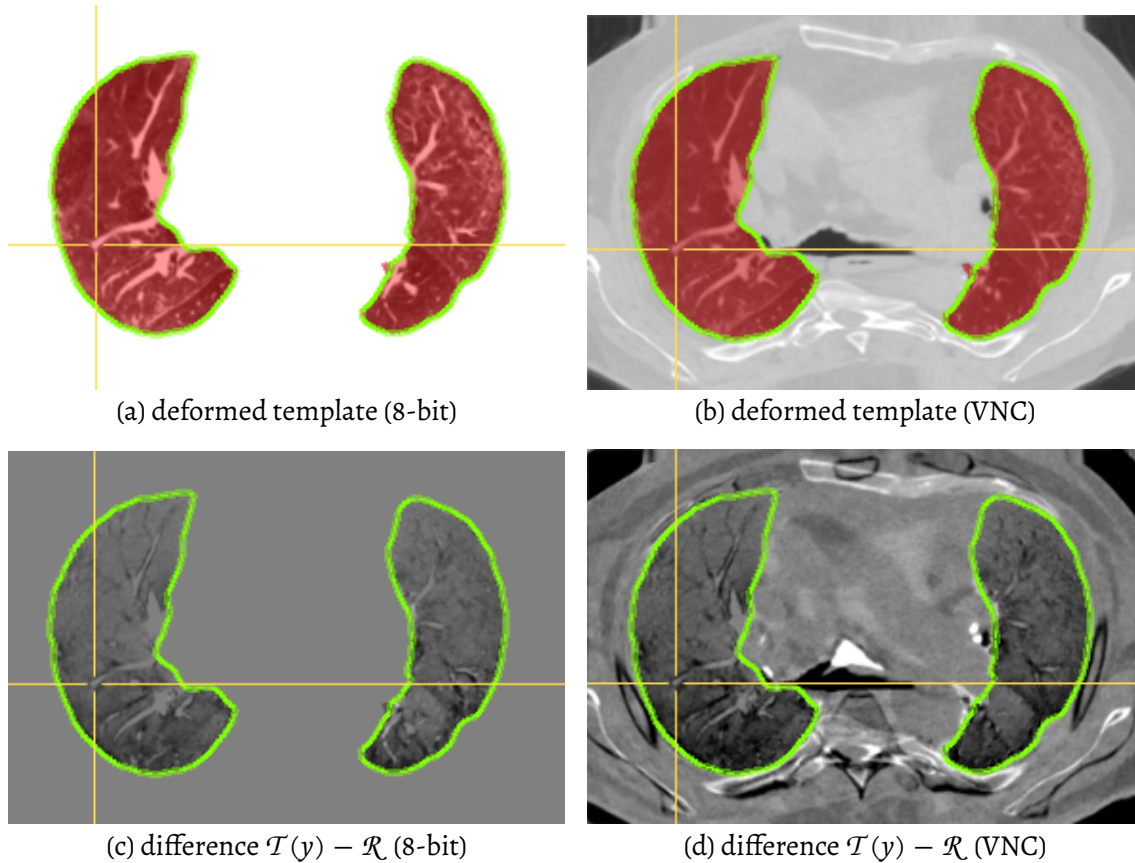


Figure 4.3: Example registration performed with NGF distance measure, curvature regularizer and $\alpha = 1$ for comparison of VNC and 8-bit input images. a)-b) show the deformed template images and c)-d) the differences of the deformed template and the reference. All images are displayed in axial view.

ment of inner structures for the VNC data set.

All in all, considering the results in table 4.1 and figure 4.3 the 8-bit images yield more suitable results for calculating reference values for regional ventilation. For the following analysis of the results only computations with the cropped 8-bit images are used.

4.2 Separated lung registration vs. whole lung registration

In order to test the first hypothesis that the separated registration of the left and right lung is more precise than registering the whole lung at once I performed all computations for the whole and the separated lung.

For comparing the error values and Jacobian determinants I calculated mean values of the results of the separated left and right registrations displaying them under the term “separated”. Additionally, I’m going to compare the runtime of the whole lung registration with the sum of the runtime of the individual registrations of the left and right lungs.

The results can be found in table 4.4 with the 4th row representing the values for the separated registration.

Whole lung vs. separated lung registration				
data set	error	volume ratio	Jacobian \pm STD	runtime in s
whole	0.03222	1.86992	1.83992 ± 0.35603	51.95
left	0.02313	1.94248	1.92433 ± 0.36019	20.89
right	0.00971	1.82033	1.8159 ± 0.33188	24.98
separated	0.01642	1.86992	1.87012 ± 0.34604	45.87

Table 4.4: Comparison of the image registration of the whole lungs and separated lungs. Note that the values for “separated” are mean values of the values for the left and right lung except for the runtime which of course is the sum of the runtime of left and right and the volume ratio which was taken from the first row for comparison.

Table 4.4 shows, that the separated registration is indeed more precise considering the error value. The error for both the right and left lung registration is smaller than the error for registering the whole lungs and therefore the mean error for the separated registration is smaller, too. Considering the Jacobian determinants the standard deviation for the separated registration is smaller implying a smoother deformation. For further analysis of the Jacobian determinants I displayed the corresponding boxplots in figure 4.5.

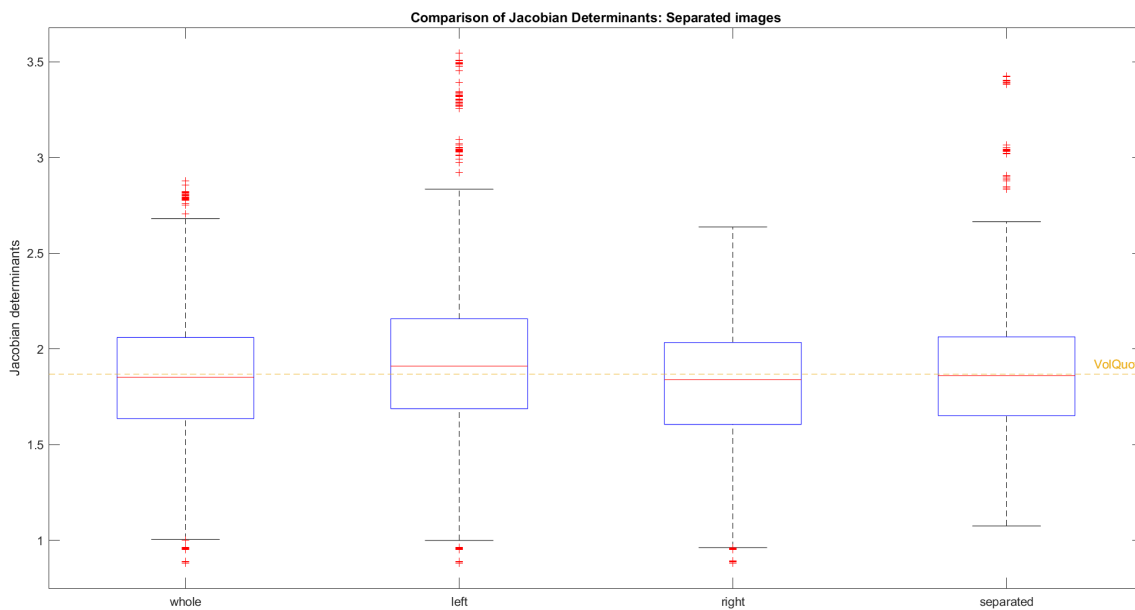


Figure 4.5: Boxplot of the Jacobian determinants over all computations using cropped 8-bit images, comparing the registration of the whole lungs with the registration of the separated left and right lungs. The yellow dashed line corresponds to the volume ratio of the whole lung.

The boxplots in figure 4.5 show that the median of the Jacobian determinants for the separated registration is closer to the volume ratio than for the registration of the whole lungs while also having a smaller deviation.

What can also be read from the boxplots is that the left lung seems to have a more complex movement than the right lung as there are more outliers and over all a wider distribution. As the left lung shares space with the heart the movement is restricted or even disturbed which lead to the stated hypothesis. As this complication in the movement of the left lung corresponds with the results in table 4.4 and figure 4.5 the separated registration is reasonable and allows for an individual optimization of the regularization term. The results of the different regularization approaches can be found in section 4.4.

4.3 SSD vs. NGF

In figure 4.3 the outliers in the VNC image set were caused by the computations using the SSD distance measure which led to the statement that SSD isn't suitable for the registration of the original unmasked images. In this section I'm going to show that NGF is the distance measure of choice for registering CT scans of the lungs as it does not depend on the absolute intensity values and instead aims for an alignment of edges.

For this experiment I used the 8-bit images, including the whole and separated lung images. The curvature regularizer with $\alpha = 1$ was employed and additionally a volume controlling term with a rational function penalty like described in section 2.4 and $\alpha_3 = 0.00125$.

The results can be found in table 4.6.

SSD vs. NGF distance measure					
image set	distance measure	error	volume ratio	Jacobian \pm STD	runtime in s
whole	SSD	0.01606	1.82155	1.80766 \pm 0.34149	43.51
	NGF	0.00640	1.82155	1.82306 \pm 0.47684	50.83
left	SSD	0.01468	1.89599	1.88226 \pm 0.37489	17.35
	NGF	0.00887	1.89599	1.89325 \pm 0.53277	18.08
right	SSD	0.00602	1.77204	1.76633 \pm 0.33923	20.63
	NGF	0.00434	1.77204	1.77536 \pm 0.44655	21.67

Table 4.6: Comparison of the two distance measures SSD and NGF. The registrations were performed using the 8-bit data set.

Although the runtime for all image sets is lower for the computations with the SSD distance measure, it isn't as precise as the one where I applied the NGF distance measure. The calculated error values are smaller using NGF implying a more precise prediction of the regional volume change by the Jacobian determinants. For further analysis of the distance measures let's have a look at an example registration.

Figure 4.7 shows that the registration for both distance measures yields a good alignment of the lung boundaries to the reference label. Regarding the differences of the de-

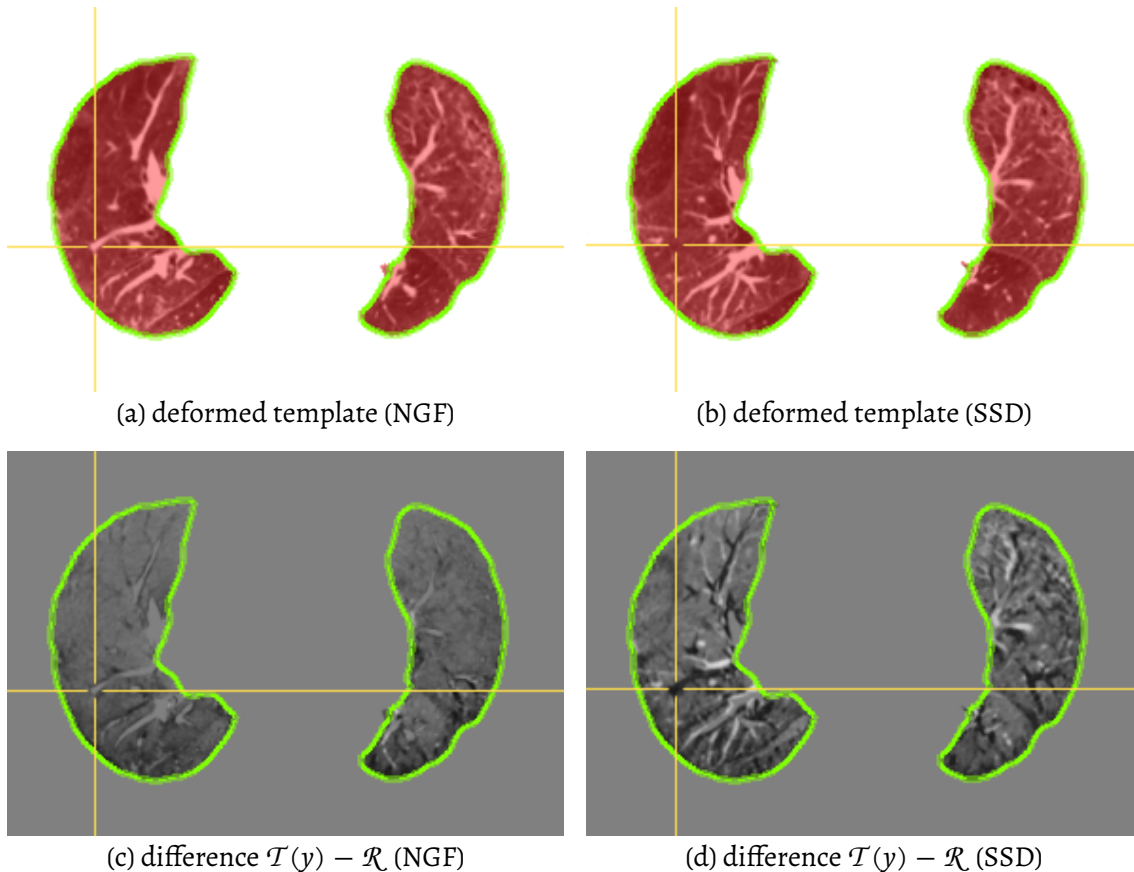


Figure 4.7: Example registration performed with curvature regularizer and volume controlling term ($\alpha = 1, \alpha_3 = 0.00125$) for comparison of the NGF and SSD distance measure. a)-b) showing the deformed template images and c)-d) the differences of the deformed template and the reference. All images are displayed in axial view.

formed template and the reference image displayed in the second row of the figure, the NGF distance measure is able to align the inner structures like blood vessels or bronchi like predicted in the hypothesis while the SSD measure fails to do that.

Looking at the Jacobians of the deformation fields in 4.8, it shows what can be seen in the differences in figure 4.7, aswell. The SSD distance measure only leads to a deformation of the lung boundaries to fit the reference label but not to a desired alignment of the inner structures. Therefore, NGF is the distance measure of choice for registering lung CT scans because it leads to a reasonable deformation of the lung tissue aligning the inner structures.

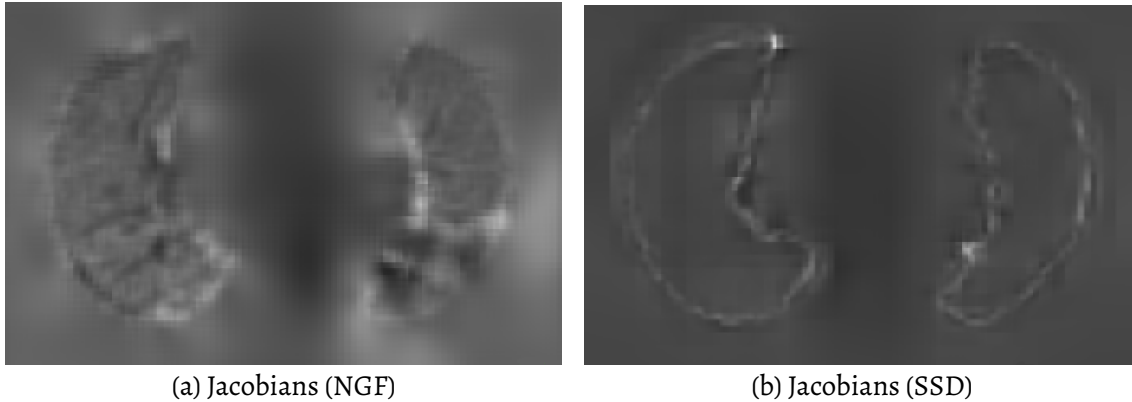


Figure 4.8: Comparison of the Jacobians of the deformation fields using NGF and SSD distance measures. The deformation fields result from the image registrations performed in figure 4.7.

4.4 Comparison of different regularization approaches

After the conclusion in section 4.2 I'm now going to compare different regularization approaches with the goal of optimizing the registration results for the left and right lungs individually.

In the tables 4.9, 4.12 and 4.15 I only listed registrations that led to an error value < 0.01 except when there weren't any values < 0.01 for one type of regularizer. In this case I listed some examples with error values above 0.01.

For the curvature and hyperelastic regularizer I tested values for α , respectively α_1 in $[0.0, 0.2, 0.4, 0.6, 0.8, 1.0, 1.2, 1.4, 1.6, 1.8, 2.0, 2.4, 2.6]$.

For α_3 I tested values in $[0.001, 0.00125, 0.0015, 0.00175, 0.002]$ but the hyperelastic regularization yielded the best results for $\alpha_3 = 0.00125893$ which was the initial weight given by the nonparametric registration module.

Like mentioned before in section 3.3, the hyperelastic regularizer usually consists of a length, surface and volume controlling term, but since the surface term is not yet implemented in MeVisLab the weight α_2 is constantly set to 0. The length controlling term coincides with the diffusive regularizer. Besides the diffusive, curvature and hyperelastic approach I additionally tested the curvature regularizer in combination with a volume controlling term with a rational function as penalty function (the same as employed in the hyperelastic regularizer).

For further analysis of the performed registrations with the smallest error I'm going to compare the registration outputs in figures 4.10, 4.13 and 4.16 and 3D bar plots of the Jacobians for one slice of the deformation in axial view including histogramms of the Jacobians in figures 4.11, 4.14 and 4.17 for each set of images.

Optimization of the Regularization for the left lung

In this paragraph I'm going to compare the different regularization approaches for the registration of the left lung.

Diffusive vs. Curvature vs. Hyperelastic (left)						
regularizer	α/α_1	α_3	error	volume ratio	Jacobian \pm STD	runtime
diffusive	1.0	0.0	0.03987	1.98896	1.95877 \pm 0.07462	26.60
hyper	0.0	0.00125893	0.01073	1.98896	1.99278 \pm 0.45362	26.73
	0.2	0.00125893	0.01842	1.98896	1.97354 \pm 0.27392	22.42
curvature	1.0	0.0	0.00673	1.98896	1.98947 \pm 0.41753	16.06
	0.4	0.00125893	0.00822	1.89599	1.89588 \pm 0.43920	23.84
	0.6	0.00125893	0.00821	1.89599	1.89449 \pm 0.41657	22.00
	0.8	0.00125893	0.00830	1.89599	1.89431 \pm 0.40210	19.63
	1.0	0.00125893	0.00887	1.89599	1.89325 \pm 0.37834	18.08
	1.2	0.00125893	0.00847	1.89599	1.89335 \pm 0.37169	17.52
	1.4	0.00125893	0.00840	1.89599	1.89320 \pm 0.34918	16.79
	1.6	0.00125893	0.00893	1.89599	1.89260 \pm 0.34654	16.72
	1.8	0.00125893	0.00927	1.89599	1.89189 \pm 0.32415	16.48
	2.0	0.00125893	0.00909	1.89599	1.89204 \pm 0.32326	16.29
	2.2	0.00125893	0.00900	1.98896	1.98597 \pm 0.29727	15.63
2.4	0.00125893	0.00893	1.98896	1.98588 \pm 0.28839	15.47	
2.6	0.00125893	0.00947	1.98896	1.98527 \pm 0.27418	15.47	

Table 4.9: Comparison of the different regularization approaches for the left lung. “Hyper” stands for the hyperelastic regularizer (diffusive + volume control term). Note that the surface controlling term is not yet implemented in MeVisLab which is why α_2 is constantly 0 and doesn't appear in the table. The best results of the error measure for each regularizer approach are marked in yellow.

Table 4.9 shows that the smallest error is achieved by the curvature regularizer with $\alpha = 1.0$ while also being faster than the other highlighted regularizations. In general the use of the curvature regularizer, whether with or without a volume controlling term, yields a smaller error than using the diffusive regularizer (or hyperelastic, which also employs the diffusive regularizer as length controlling term). The errors for the hyperelastic regularizer were higher than 0.01 for every performed registration whereas the curvature regularizer almost always (except for $\alpha = 0.0$ and $\alpha = 0.2$, which therefore are not displayed in the table) generated a value below 0.01.

The smallest deviation is given by the diffusive regularizer which also has the biggest error. This implies that the diffusive regularizer overall leads to a rather weak deformation and the registration result is not expected to be reasonable. It is also noticeable that the deviation of the Jacobians gets smaller with increasing the regularization weight α and therefore increasing the smoothness of the resulting transformation.

For further interpretation of the registration results, let us have a look at the deformed template and difference images in figure 4.11.

What catches the eye first when looking at the deformed template images $\mathcal{T}(y)$ in figure 4.10 is that the one generated by the diffusive regularizer does not fit the reference label very well and there is a lot of overhang compared to the others.

Regarding the difference images, the best job at aligning the inner structures of the lungs does the curvature with volume control approach, which can be best seen at the branching targeted by the cursor.

Finally, I'm going to compare the Jacobians themselves in form of 3D bar plots resembling the deformation for one slice in axial view and histograms of the Jacobians in figure 4.11.

The color coding chosen for the 3D bar plots shows that all deformations in 4.11 are reasonable in the sense of the regional volume change, because the majority of Jacobians imply volume expansion or no volume change which is expected when choosing the expirational image as reference.

The hyperelastic regularization displayed in subplot c) does not result in a smooth deformation. Since the smallest error was given for $\alpha_1 = 0.0$ a diffeomorphic deformation is not guaranteed because the length controlling term of the hyperelastic regularization has been diminished.

As expected the diffusive regularizer approach in a) results in a overall weak deformation and the small deviation can be seen in the histogram which shows a really steep peak at approximately 1.9.

Both approaches using the curvature regularizer generated smooth deformations. Although the error for the curvature regularizer without volume controlling term is smaller, the one with volume controlling term displayed in g) better reflects the structure of the left lung. I noticed that the deformation resulting from the curvature regularizer in e) sort of "leaks" into the background so that the shape of the lung is not completely visible. Whereas the deformation in g) is able to not only resemble the shape of the left lung but also the fissure dividing the lung into two lobes is visible.

After comparing these different approaches I choose the curvature regularizer including a volume controlling term with $\alpha_1 = 0.6$ and $\alpha_3 = 0.00125893$ as the best approach and a good compromise between error minimization, computing time and reasonability regarding the research goal.

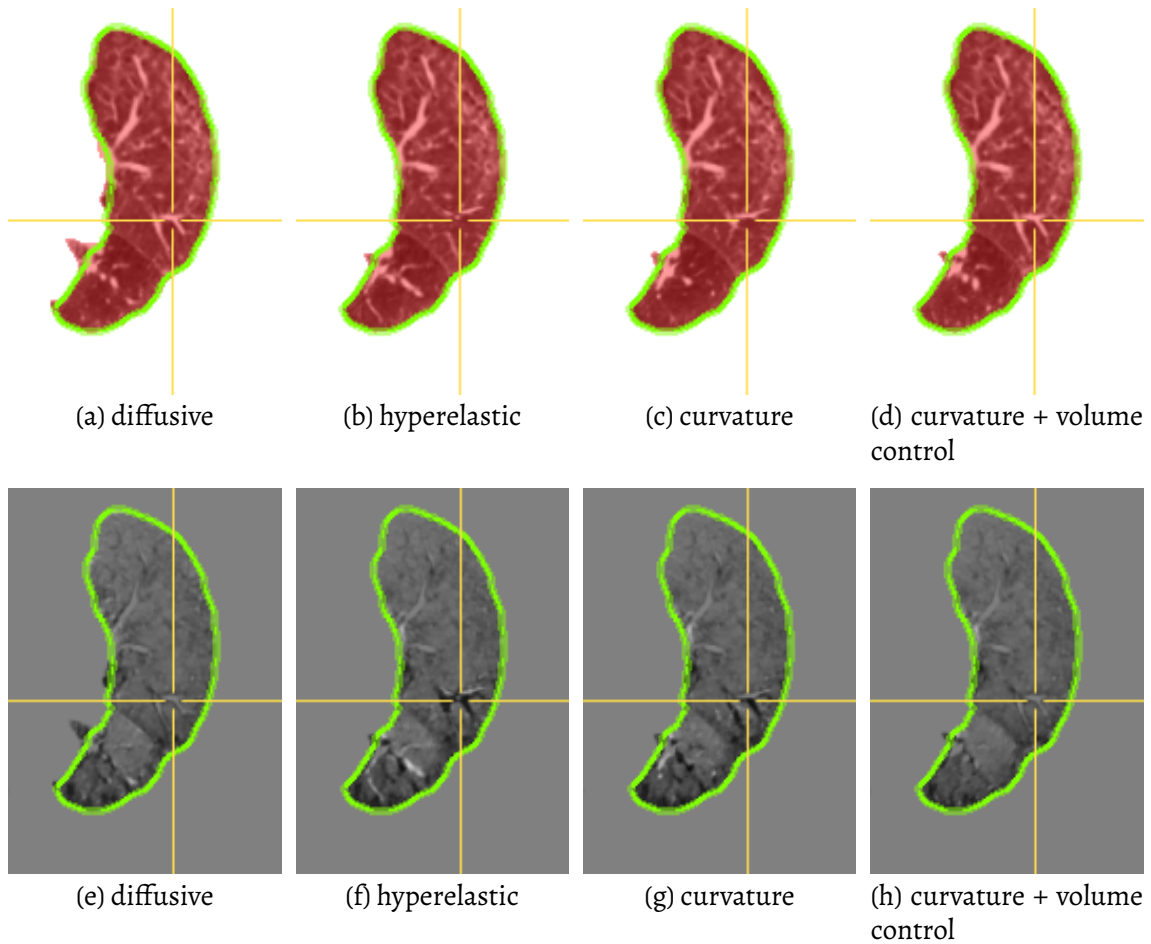


Figure 4.10: Registration outputs of the different registration approaches highlighted in table 4.9. a)-d): deformed template images $\mathcal{T}(y)$, e)-h): the difference of the deformed template and reference images $\mathcal{T}(y) - \mathcal{R}$. From left to right: diffusive with $\alpha = 1.0$, hyperelastic with $\alpha_1 = 0.0$ and $\alpha_3 = 0.00125893$, curvature with $\alpha = 1.0$ and curvature + volume controlling term with $\alpha_1 = 0.6$ and $\alpha_3 = 0.00125893$. The cursor points at corresponding voxels.

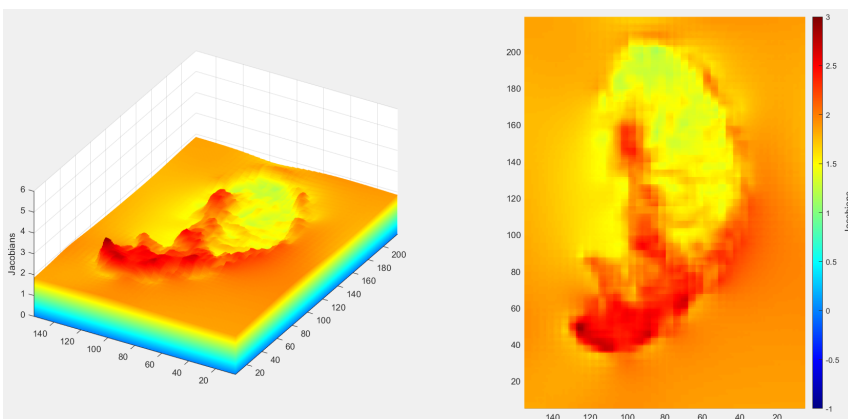
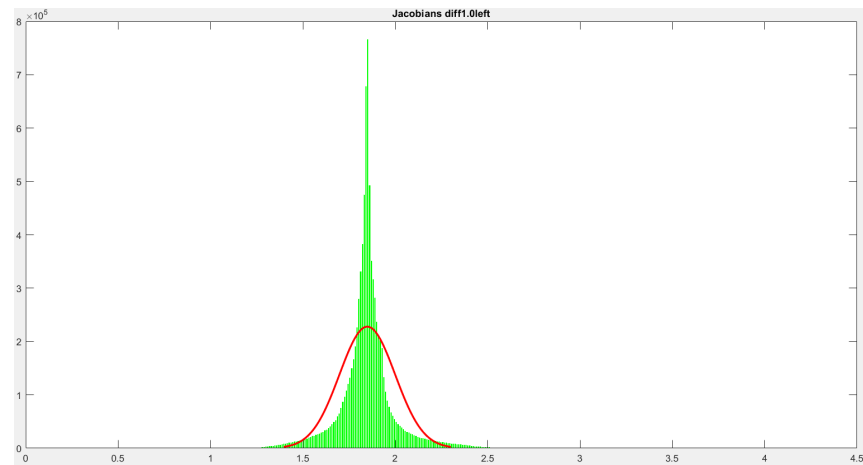
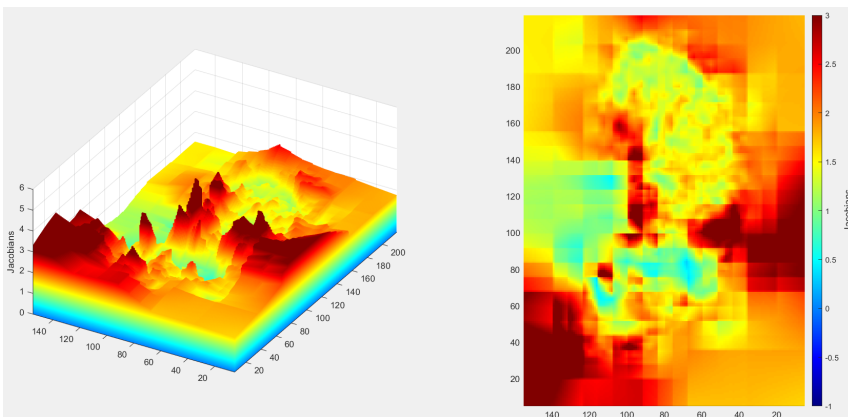
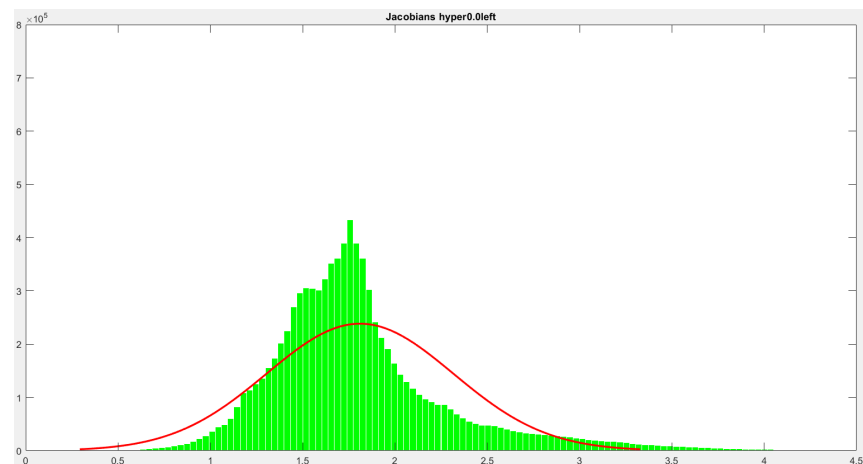
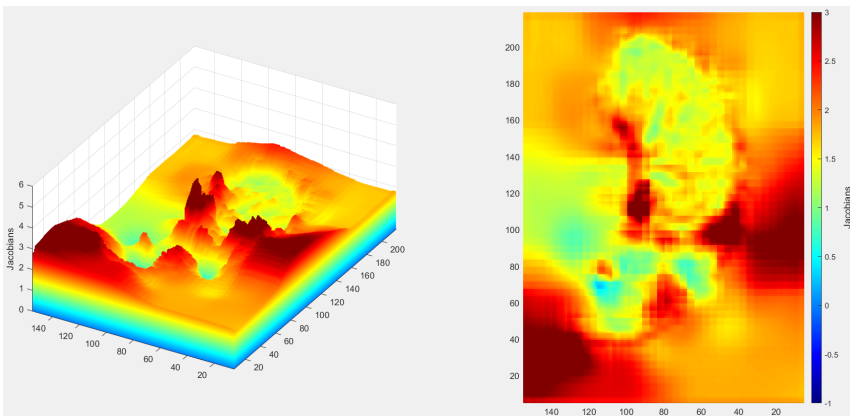
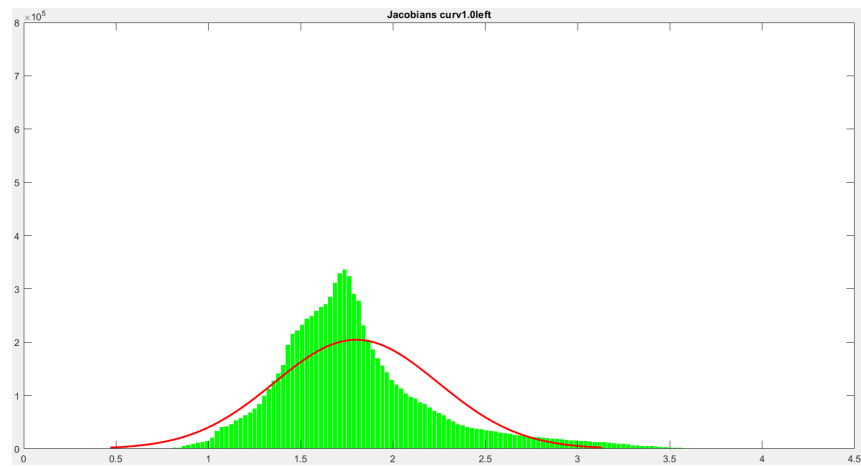
(a) Diffusive regularizer with $\alpha = 1.0$, error=0.03987(b) Histogramm of the Jacobians for $\alpha = 1.0$ (c) Hyperelastic regularizer with $\alpha_1 = 0.0$ and $\alpha_3 = 0.00125893$, error=0.01073(d) Histogramm of the Jacobians for $\alpha_1 = 0.0$ and $\alpha_3 = 0.00125893$

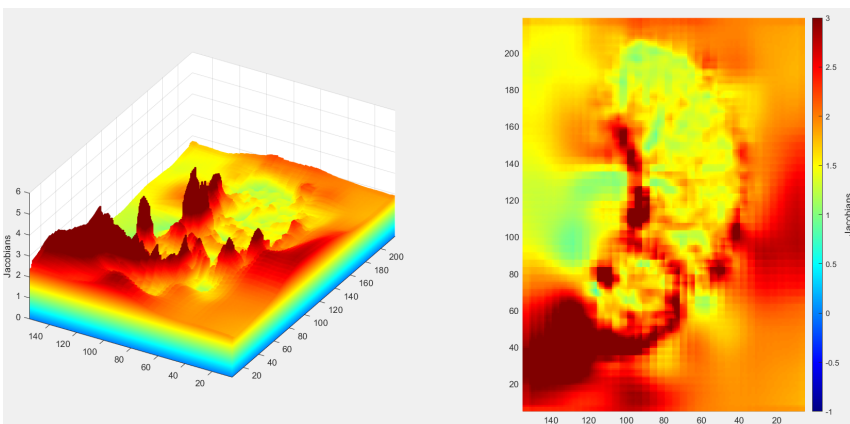
Figure 4.11: **left:** 3D bar plots of the Jacobians for comparison of the three regularization approaches that had the smallest error for registering the left lung. A Jacobian of 1 represented by green coloring indicates no volume change, a Jacobian higher than 1 represented in warm colors (yellow and red) indicates volume expansion and Jacobians between 0 and 1 represented with blue coloring indicates volume shrinkage. **right:** histogramm of the Jacobians and fitted normal density function in red.



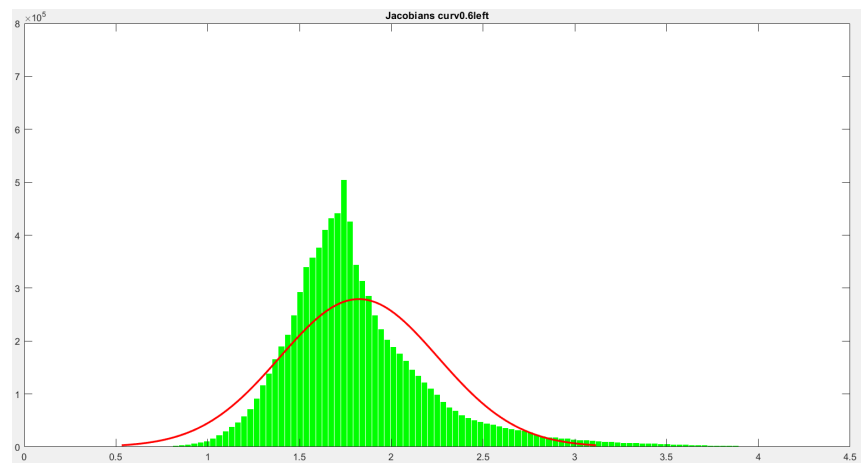
(e) Curvature regularizer with $\alpha = 1.0$, error=0.00673



(f) Histogramm of the Jacobians for $\alpha = 1.0$



(g) Curvature regularizer with $\alpha_1 = 0.6$ and volume control term with $\alpha_3 = 0.00125893$, error=0.00821



(h) Histogramm of the Jacobians for $\alpha_1 = 0.6$ and $\alpha_3 = 0.00125893$

Optimization of the Regularization for the right lung

After looking at the registration results for the left lung I will now compare the different regularization approaches for the right lung.

The tables and figures are analogous to the ones for the left lung.

Diffusive vs. Curvature vs. Hyperelastic (right)						
regularizer	α/α_1	α_3	error	volume ratio	Jacobian \pm STD	runtime
diffusive	1.0	0.0	0.01643	1.86863	1.86326 \pm 0.07712	31.65
hyper	0.0	0.00125893	0.00761	1.86863	1.87616 \pm 0.33522	33.47
	0.2	0.00125893	0.00523	1.86863	1.86780 \pm 0.23431	27.31
	0.4	0.00125893	0.00888	1.86863	1.86494 \pm 0.16605	22.40
curvature	1.0	0.0	0.00419	1.86863	1.8722 \pm 0.27208	19.70
	0.0	0.00125893	0.00679	1.77204	1.77861 \pm 0.29682	31.76
	0.2	0.00125893	0.00623	1.77204	1.77789 \pm 0.28923	30.94
	0.4	0.00125893	0.00522	1.77204	1.77663 \pm 0.27945	29.35
	0.6	0.00125893	0.00465	1.77204	1.77594 \pm 0.26597	25.08
	0.8	0.00125893	0.00449	1.77204	1.77560 \pm 0.24807	22.65
	1.0	0.00125893	0.00434	1.77204	1.77536 \pm 0.23306	21.67
	1.2	0.00125893	0.00435	1.77204	1.77525 \pm 0.22542	21.08
	1.4	0.00125893	0.00416	1.77204	1.77496 \pm 0.21346	20.01
	1.6	0.00125893	0.00408	1.77204	1.77484 \pm 0.20592	19.77
	1.8	0.00125893	0.00407	1.77204	1.77463 \pm 0.19939	19.18
	2.0	0.00125893	0.00412	1.77204	1.77449 \pm 0.19264	19.06
	2.2	0.00125893	0.00400	1.86863	1.87121 \pm 0.20749	18.43
2.4	0.00125893	0.00404	1.86863	1.87106 \pm 0.20207	18.74	
2.6	0.00125893	0.00405	1.86863	1.87098 \pm 0.19747	20.51	

Table 4.12: Comparison of the different regularization approaches for the right lung. “Hyper” stands for the hyperelastic regularizer (diffusive + volume control term). Note that the surface controlling term is not yet implemented in MeVisLab which is why α_2 is constantly 0 and doesn’t appear in the table. The best results of the error measure for each regularizer approach are marked in yellow.

Looking at table 4.12, the smallest error is given by the curvature regularizer with volume controlling term with $\alpha_1 = 2.2$ and $\alpha_3 = 0,00125893$. Additionally, this approach also yielded the shortest computation time.

Analogously to the left lung registration, the smallest deviation of the Jacobian determinants is given by the diffusive regularizer.

Comparing the registration of the two lung halves, the registration of the right lung leads to a smaller error in general while having a longer computation time. On one hand this is due to the expected more complex movement of the left lung and on the other hand the right lung is bigger as the left lung in general and therefore it takes more time to compute the deformation.

What is also interesting to see, is that the smallest error for the hyperelastic regularization approach is achieved by $\alpha_1 = 0.2$ for the right lung and therefore we expect a much smoother deformation as the one generated by the hyperelastic regularizer for the left lung.

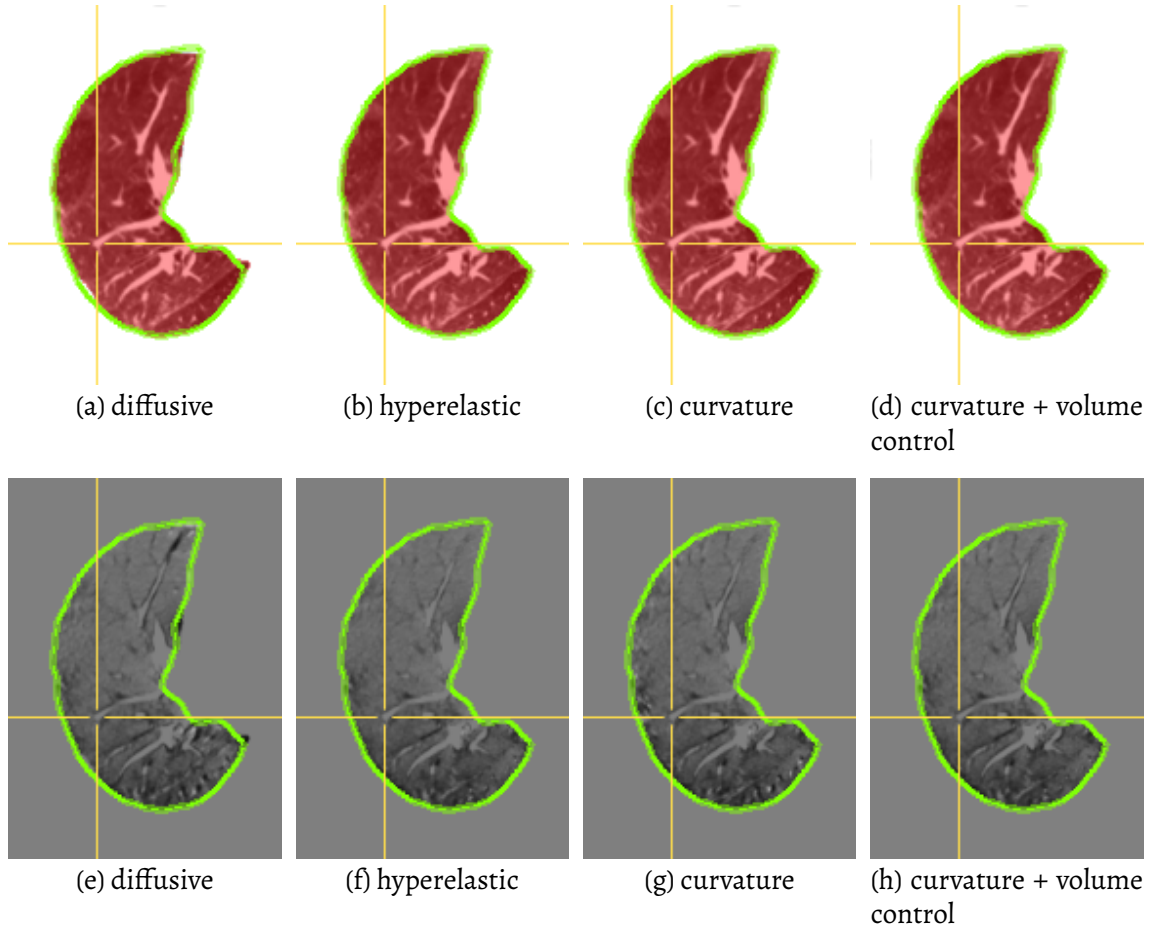
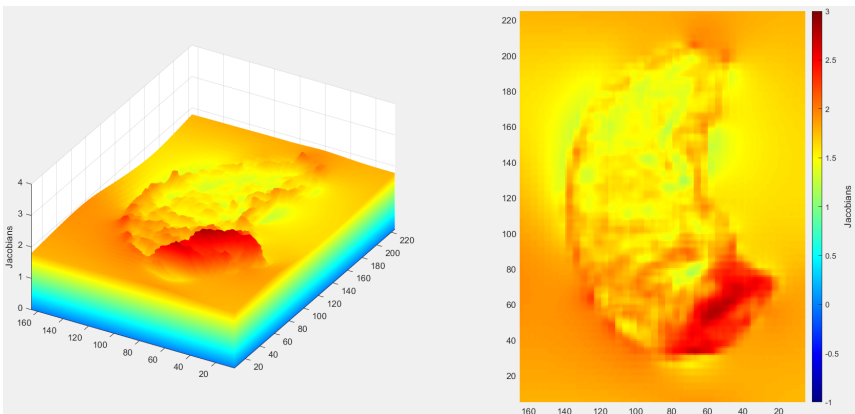


Figure 4.13: Registration outputs of the different registration approaches highlighted in table 4.12. a)-d) show the deformed template images $\mathcal{T}(y)$ and e)-h) the difference of the deformed template and reference images $\mathcal{T}(y) - \mathcal{R}$. From left to right: diffusive with $\alpha = 1.0$, hyperelastic with $\alpha_1 = 0.2$ and $\alpha_3 = 0.00125893$, curvature with $\alpha = 1.0$ and curvature + volume controlling term with $\alpha_1 = 2.2$ and $\alpha_3 = 0.00125893$. The cursor points at corresponding voxels.

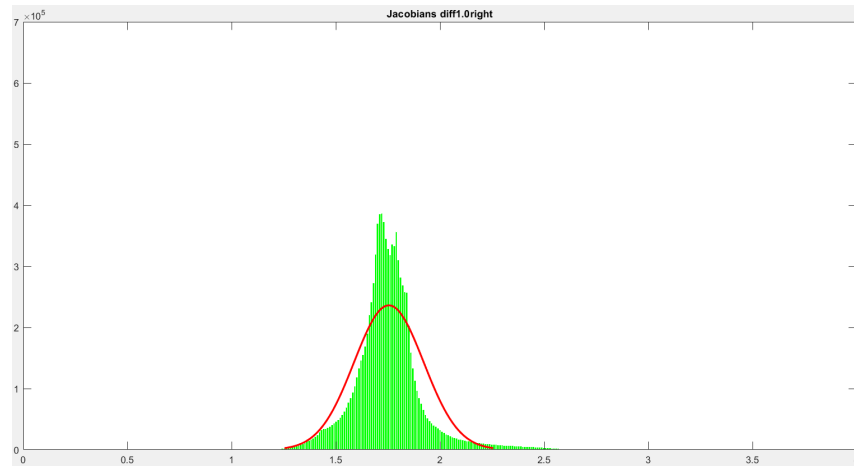
Comparing the registration outcomes in figure 4.13 the deformed template image generated by the diffusive regularizer, similar to the results in figure 4.10 for the left lung, does not fit the reference label very well compared to the other approaches.

Regarding the difference images, for the right lung the small inner structures of the lungs are best aligned by the hyperelastic and curvature with volume control regularizations resulting in relatively even difference images compared to the others. In fact, it is hard to spot a difference between the difference images in f) and h).

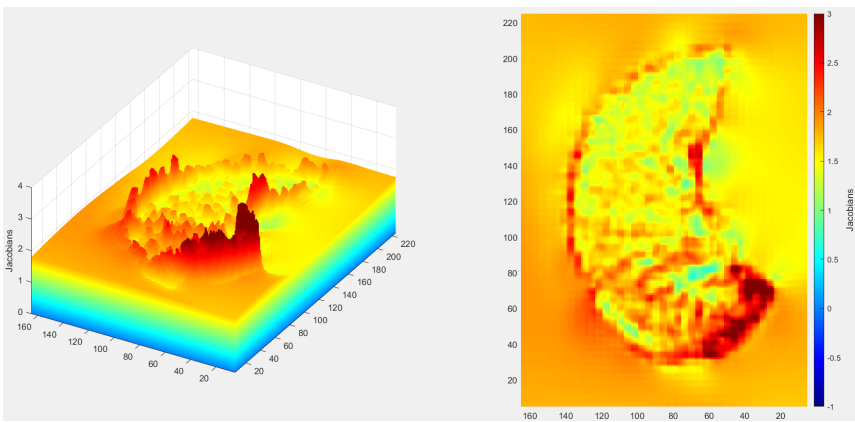
To further compare these two regularization methods, let's have a look at figure 4.14.



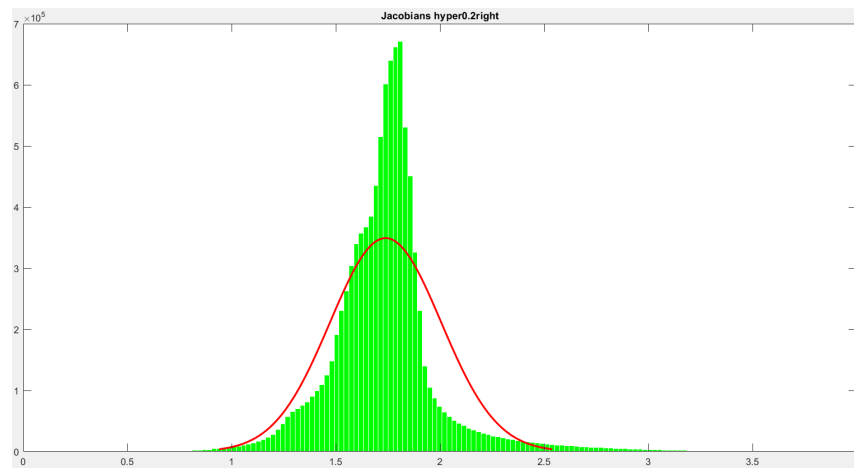
(a) Diffusive regularizer with $\alpha = 1.0$, error=0.016453



(b) Histogramm of the Jacobians for $\alpha = 1.0$

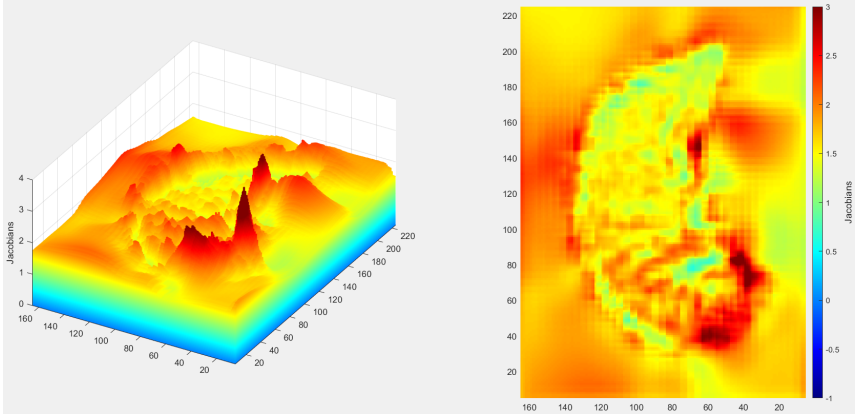


(c) Hyperelastic regularizer with $\alpha_1 = 0.2$ and $\alpha_3 = 0.00125893$, error=0.00523

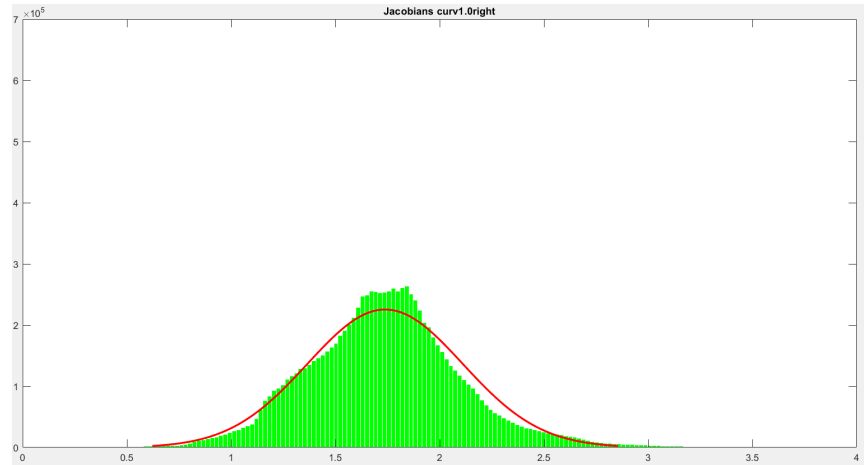


(d) Histogramm of the Jacobians for $\alpha_1 = 0.2$ and $\alpha_3 = 0.00125893$

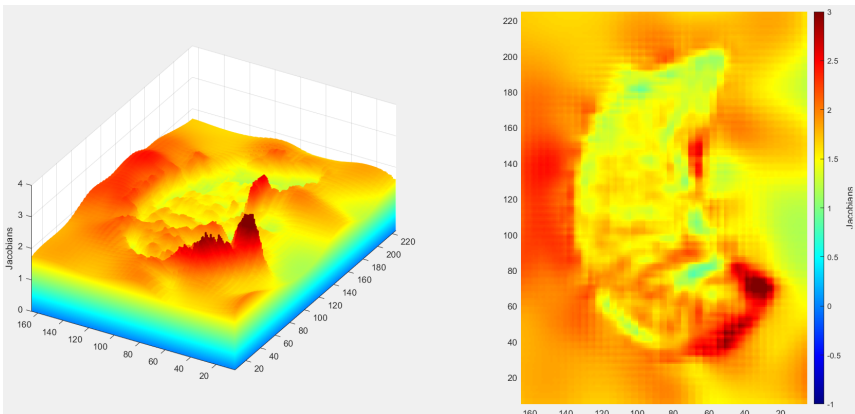
Figure 4.14: **left:** 3D bar plots of the Jacobians for comparison of the three regularization approaches that had the smallest error for registering the right lung. A Jacobian of 1 represented by green coloring indicates no volume change, a Jacobian higher than 1 represented in warm colors (yellow and red) indicates volume expansion and Jacobians between 0 and 1 represented with blue coloring indicates volume shrinkage. **right:** histogramm of the Jacobians and fitted normal density function in red.



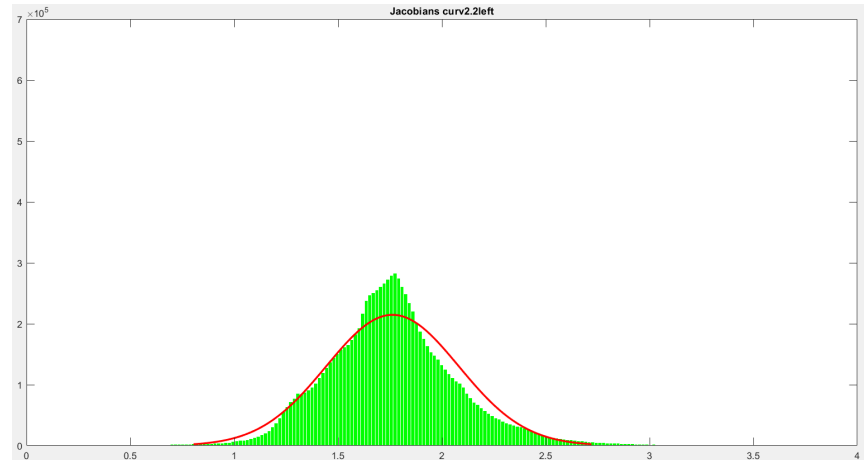
(e) Curvature regularizer with $\alpha = 1.0$, error=0.00149



(f) Histogramm of the Jacobians for $\alpha = 1.0$



(g) Curvature regularizer with $\alpha_1 = 2.2$ and volume control term with $\alpha_3 = 0.00125893$, error=0.00400



(h) Histogramm of the Jacobians for $\alpha_1 = 2.2$ and $\alpha_3 = 0.00125893$

The deformations displayed as 3D bar plots in figure 4.14 are all relatively smooth compared to the ones of the left lung in figure 4.11.

The behavior of the transformations generated by the diffusive and curvature regularizer is analogous to the ones of the left lung. Although the registrations of the right lung generally led to better outcomes (more precise alignment) than the registrations of the left lung.

As I mentioned earlier while describing the difference images in figure 4.13, the best alignment of inner structures is achieved by the hyperelastic regularizer and the curvature regularizer with volume controlling term. Therefore, I will now have a closer look at the Jacobians of the deformations generated by these two methods.

The biggest difference that meets the eye is along the boundary of the lung. The Jacobians in c) imply volume expansion along the lung boundary (meaning the most outward lung tissue inside of the pleural sack), whereas the Jacobians in g) imply no volume change or small volume expansion along the boundary. Since we expect the main expansion of the lungs take place in the internal lung tissue rather than the tissue along the boundary as the outward expansion is limited by the pleural sack and rib cage, the deformation yielded by the curvature regularizer with volume control seems more reasonable.

Best separated Registration vs. best registration of the whole lungs

I analogously investigated the results for the whole lung and will briefly list the best regularization approaches in table 4.15.

After I compared the image registration results and the 3D bar plots and histograms of the Jacobians I came to the conclusion that the approach with curvature regularizer and volume controlling term leads to the most reasonable deformation for the whole lungs, aswell. For this type of regularization the smallest error was achieved for $\alpha_1 = 2.4$ and $\alpha_3 = 0.00125893$.

The corresponding plots can be found in figure 4.16 and 4.17.

Diffusive vs. Curvature vs. Hyperelastic (whole)						
regularizer	α/α_1	α_3	error	volume ratio	Jacobian \pm STD	runtime
diffusive	1.0	0.0	0.06224	1.91829	1.85652 \pm 0.06807	66.23
hyper	0.0	0.00125893	0.00841	1.91829	1.92342 \pm 0.32815	63.04
curvature	1.0	0.0	0.00503	1.91829	1.92096 \pm 0.35558	39.84
	2.4	0.00125893	0.00576	1.91829	1.91919 \pm 0.23891	47.83

Table 4.15: Listing of the regularization approaches with the smallest error for the whole lung. “Hyper” stands for the hyperelastic regularizer (diffusive + volume control term). Note that the weight for the surface controlling term α_2 is constantly 0 and doesn't appear in the table.

Finally, I will compare the best image registration of the whole lung with the best separated registration individually optimized for the left and right lung. Since the research goal is to use the Jacobian determinants to predict the regional volume change I will compare the registration of the whole lung with the separated registration on a more regional level. Therefore, I will list the registration results for the 5 lung lobes (region 1-5)

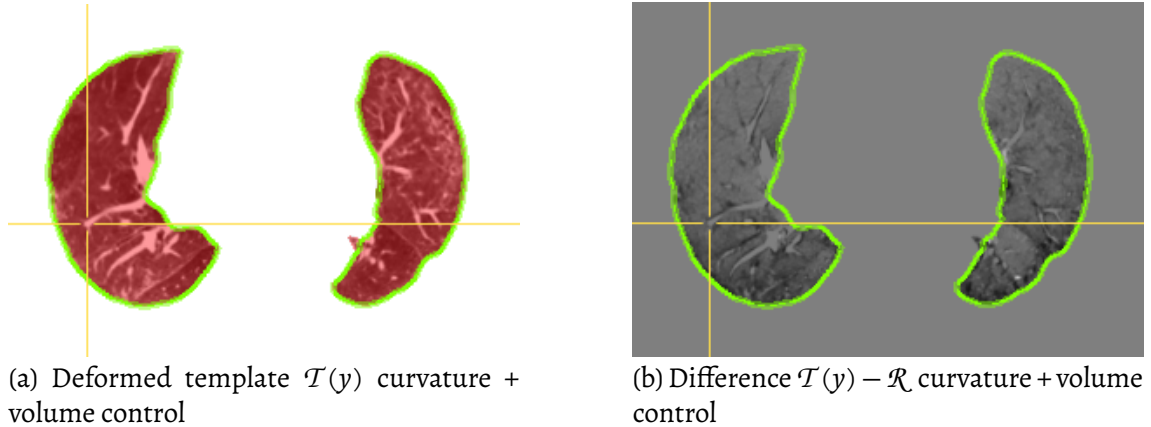


Figure 4.16: Registration outputs for $\alpha_1 = 2.4$ and $\alpha_3 = 0.00125893$. The cursor points at corresponding voxels.

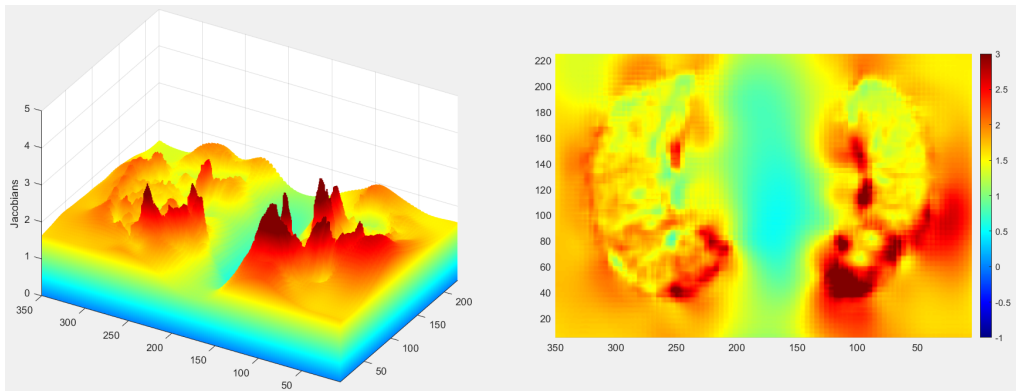
in order to see if the separated registration of the lungs yields a more precise prediction of volume change on a regional level than the registration of the whole lung.

The tables 4.18-4.22 show, that the error for the lung lobes 2,3 and 4 could be reduced by the separated registration.

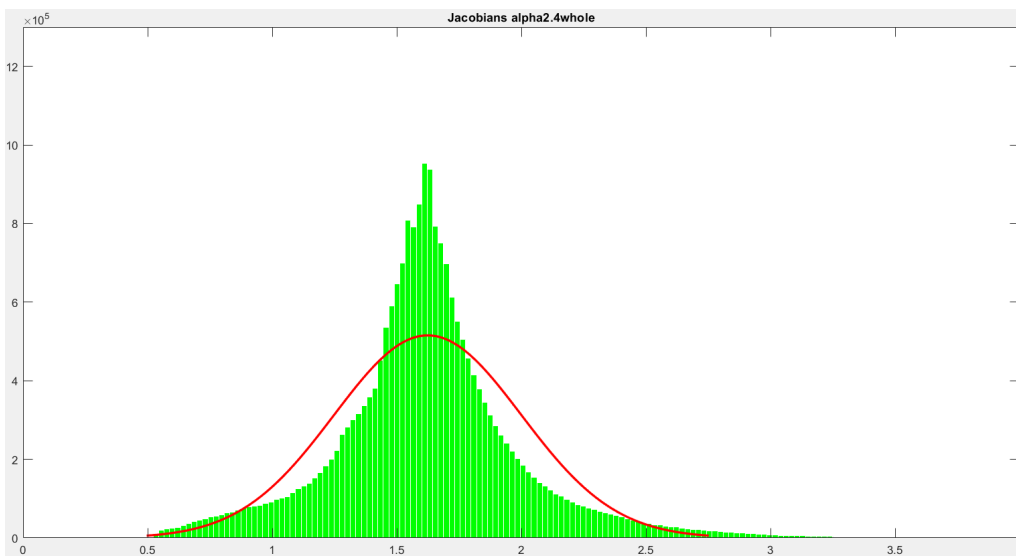
What can also be read from the tables is that the lung lobe labeled with 5 in the left lung caused the largest error. It is also where the most movement or regional volume change takes place as the volume ratio is higher than 2 implying an expansion to more than twice the initial volume in expiration.

As a conclusion the separated registration shows the potential of a more regional registration in order to get a more precise prediction for regional volume change and therefore an individual registration of the 5 lung lobes comes into consideration.

4 Results



(a) Curvature regularizer with $\alpha_1 = 2.4$ and volume control term with $\alpha_3 = 0.00125893$, error=0.00576



(b) Histogramm of the Jacobians for $\alpha_1 = 2.4$ and $\alpha_3 = 0.00125893$

Figure 4.17: 3D bar plot and histogramm of the Jacobians of the best regularization approach for the whole lung. A Jacobian of 1 represented by green coloring indicates no volume change, a Jacobian higher than 1 represented in warm colors (yellow and red) indicates volume expansion and Jacobians between 0 and 1 represented with blue coloring indicates volume shrinkage. A normal density function (red) is fitted to the histogramm.

Separated vs. whole lung registration region 1

registration method	error	volume ratio	Jacobian \pm STD
whole	0.04851	1.84888	1.85896 \pm 0.16260
separated	0.05012	1.84888	1.85988 \pm 0.17791

Table 4.18: Results for the separated and whole lung registration in region 1 (lung lobe labeled with 1 in the right lung)

Separated vs. whole lung registration region 2

registration method	error	volume ratio	Jacobian \pm STD
whole	0.09383	1.78471	1.73967 \pm 0.14236
separated	0.08727	1.78471	1.73952 \pm 0.12965

Table 4.19: Results for the separated and whole lung registration in region 2 (lung lobe labeled with 2 in the right lung)

Separated vs. whole lung registration region 3

registration method	error	volume ratio	Jacobian \pm STD
whole	0.05159	1.95803	1.98281 \pm 0.22348
separated	0.04783	1.95803	1.98274 \pm 0.23707

Table 4.20: Results for the separated and whole lung registration in region 3 (lung lobe labeled with 3 in the right lung)

Separated vs. whole lung registration region 4

registration method	error	volume ratio	Jacobian \pm STD
whole	0.06084	1.94613	1.90859 \pm 0.18858
separated	0.05313	1.84431	1.81014 \pm 0.26676

Table 4.21: Results for the separated and whole lung registration in region 4 (lung lobe labeled with 4 in the left lung)

Separated vs. whole lung registration region 5

registration method	error	volume ratio	Jacobian \pm STD
whole	0.10826	2.06559	2.12049 \pm 0.37941
separated	0.12210	2.04086	2.06673 \pm 0.66660

Table 4.22: Results for the separated and whole lung registration in region 5 (lung lobe labeled with 5 in the left lung)

5

Discussion and Conclusion

In this chapter I will conclude the results I presented in the chapter before and discuss the hypotheses from section 2.7 as well as the execution of the experiments. Additionally, I'm going to comment on the research goal and the outlook regarding the research project.

5.1 Discussion

In this section I will first discuss the outcomes for the different hypotheses I set up before the experiments, then I will go into detail about the execution of the experiments and critically assess my approaches.

Hypothesis 1: separated vs. whole lung registration

Regarding the first hypothesis the results in section 4.2 and 4.4 show, that the separated registration overall leads to a smaller error and faster computation. Additionally, the separated registration allows for an individual optimization for the left and right lung. The results in tables 4.9 and 4.12 confirm that the left and right lung in fact differ in their behavior. While the registration of the right lung seems relatively stable in the sense that the different regularization approaches yield comparably good registration results for all tested parameters, the registration of the left lung seems more complex and therefore the registration results vary more.

All observations indicate that a separated registration is reasonable and can lead to a more precise representation of the regional volume change of the lungs. Although the results tend to support the hypothesis I would even suggest a lobe-wise registration, especially for the left lung to see if the approach of a more regional registration is reasonable regarding the research goal.

Hypothesis 2: VNC vs. 8-bit images

The idea behind the second hypothesis was to simulate the features of the pleural sack by masking the images with the corresponding labels and therefore prevent folding at the boundary of the lungs. Additionally, by converting the images into a 8-bit format we

wanted to achieve a reduction of the required memory space and an improvement of the alignment of the inner structures like blood vessels and bronchi as the 8-bit images are higher in contrast. Higher contrast implies stronger edges of the small structures which then can be aligned more easily.

The results in section 4.1 showed that the registration of the 8-bit images led to a smaller error and deviation implying a smoother deformation. The examples for the deformed template and difference images in figure 4.3 showed that the registration outcomes are similar but the registration of the 8-bit image was more precise. More precise in the sense that the overhang of the deformed template and the reference label was smaller and there were less deviations in the alignment of the inner structures.

Therefore, the results strengthened the hypothesis.

Hypothesis 3: Regularization

The most reasonable results were achieved by the curvature regularizer with an added volume controlling term.

Against the expectations, the hyperelastic approach did not lead to a faster computation time or a significantly smaller error. One problem that occurred with the defined error measure was that the best results for left (and whole) lung were achieved by the hyperelastic regularizer with $\alpha_1 = 0.0$. Since the error measures the distance between the actual volume ratio and the mean Jacobian value it is expected that a registration only regularized by a volume controlling term yields a good prediction of the regional volume change but in this case it did not lead to a smooth deformation. For the registration of the right lung the hyperelastic regularizer achieved the best result for $\alpha = 0.2$ and therefore led to a smoother deformation as for the left lung which can be seen in figure 4.14 showing the potential of the hyperelastic approach. I could not show that the hyperelastic regularizer is better or more precise for pulmonary image registration and predicting the regional volume change than the other approaches.

The curvature regularization with volume control overall provided satisfying registration results and low computation time, which is analogous to the regularization approach employed by the authors of (Ruhaak et al., 2017) whose algorithm ranked first in the EM-PIRE10 challenge.

Hypothesis 4: NGF vs. SSD

Since the lung CT scans do not meet the requirements for the SSD distance measurement because the absolute intensity values of the expirational and inspirational images are not comparable due to the change in density caused by the inflowing air, it was expected that a registration with SSD does not yield a good alignment of the inner structures of the lungs.

This assertion could be verified in figures 4.7 and 4.8 and I could also show that the NGF distance measure is suitable for lung image registration strengthening the hypothesis.

Experiments

Regarding the performed experiments I'm going to address some sources of errors and challenges I had to overcome during the process.

First, the error measure I defined for the experiments was chosen based on the idea that the mean value of the Jacobian determinants should be equal to the volume ratio of the inspirational and expirational lungs. The definition I chose was simple and all in all the registration approaches resulting in a reasonable deformation also lead to a small error. A drawback of this error measure was that a small error value did not guarantee a transformation with good features (e.g. continuous, diffeomorphic) and therefore leading to unsatisfying results (see results for diffusive and hyperelastic regularizer). In order to investigate the volume change on a more regional level an error measure based on the lung lobes, e.g. comparing the volume ratio and mean Jacobian for the individual lung lobes, could be purposeful. Another idea was to include information about the distances of adjacent Jacobians in order to penalize unsmooth deformations.

Considering the optimization of the regularization I could have tested more parameters at smaller intervalls by first testing the parameters on a small batch of images beforehand instead of using all available patient data. Additionally, it would have been interesting to see a comparison of the different regularization approaches on an example that yields an above average error.

One challenge I had to overcome was that due to technical issues during the experiments I lost some of the patient data (CT scans taken at follow-up examination) which is why the volume ratio in the results varies. I decided to include the volume ratio in all tables so that it can be compared to the mean value of the Jacobians. This could imply that some of the results are biased. Since the error values of the smaller data set do not vary much from the results of the original data set and I still used data from every patient the results still seem significant. An idea to clear up the results would be to consider only every second result of the 138 patient data, thus reducing the data set to 69 patients for the analysis. Leaving out the follow-up examinations would lead to uniform volume ratios (since the follow-up data got lost), thus I would have been able to repeat the experiment with more patient data afterwards.

Nevertheless, the experiments led to reasonable and satisfying results.

In conclusion, besides the implementation of the previously missing surface controlling term of the hyperelastic regularization approach in MeVisLab it would be interesting to see if a lobe-wise registration potentially leads to a more precise prediction of the regional volume change of the lungs. Finally, defining a more complex error measure could be useful to better detect reasonability of the computed deformations.

5.2 Conclusion of the Research Goal

To answer the research question of this thesis if the mathematical model of image registration is able to simulate the pulmonary movement in such a way that the resulting Jacobian determinants of the deformation field can serve as a surrogate for regional ven-

tilation, I would say yes. Although there is no option to compare the computed deformation with some sort of groundtruth or actual movement of the lungs I could show that the registration network is able to register the lungs in an efficient and precise way. The optimized registration network was able to generate mean error values below 0.01 for a total of 138 sets of patient data where the error value represents the average distance between the by the Jacobians predicted volume ratio and the actual volume ratio of the lungs. The fact that researchers could already show that CT-based regional ventilation has the potential to serve as an early imaging marker for various lung diseases (Fuld et al., 2008) (Scharm et al., 2021) suggests that the clinical use of precise and efficient pulmonary imaging registration could have a significant effect on the diagnosis of these diseases. For further validation of the results produced within this thesis a comparison of the results with the pulmonary function test data of the patients is planned. Additionally, the efficiency of the registration network (precision and speed) will be compared with a prototype implemented in ANTs (Advanced Normalization Tools).

5.3 Outlook

Finally, in this section I'm going to give a short outlook on what are the next steps for this research project and conclude this thesis in a few sentences.

As I already mentioned in the introduction, one goal of this research project is to integrate the image registration network into an automatic work flow to process large amounts of patient data. This will include the automatic preprocessing of the CT scans and generated label images, the pulmonary image registration network with the Jacobian determinants as output and a visualization using ITK-SNAP (Yushkevich et al., 2006). This work flow will be used for a clinical study on healthy patients in order to calculate reference values for regional ventilation of the lungs. The ultimate goal is to implement a software application for CT scanners that simplifies the detection of abnormalities of the lung ventilation indicated by deviation from the reference values generated by the clinical study. Whether this finally leads to a faster diagnosis and therefore to a better outcome for the patients has to be shown in follow-up studies comparing the novel registration-based diagnosis tool to the standard procedure.

Additionally, the tool can be extended for example by adding lung perfusion information in order to cover more types of diseases.

In conclusion, this thesis presented reasonable results for pulmonary image registration generating a good representation of the volume change by the Jacobian determinants. The results also reflected how crucial the choice of the mathematical model and especially the choice of the regularization is in order to get reasonable outcomes. In the future of imaging-based diagnosis image registration has the potential to be employed in many other clinical applications.

Bibliography

- Bertsekas, D.P. (1995). *Nonlinear Programming*. Athena Scientific. ISBN: 978-1-886-52914-4.
- Broit, C. (1981). *Optimal registration of deformed images*. English. ID: 13816609. PhD thesis.
- Burger, M., Modersitzki, J., and Ruthotto, L. (2013). A hyperelastic regularization energy for image registration. *SIAM journal on scientific computing* 35, B132–B148. URL: <https://search.proquest.com/docview/1270328216>.
- Buzug, T.M. (2004). *Einführung in die Computertomographie*. Springer Berlin Heidelberg. ISBN: 978-3-642-62184-0. DOI: 10.1007/978-3-642-18593-9.
- Castillo, R., Castillo, E., Fuentes, D., Ahmad, M., Wood, A.M., Ludwig, M.S., and Guerrero, T. (2013). A reference dataset for deformable image registration spatial accuracy evaluation using the COPDgene study archive. *eng. Physics in Medicine and Biology* 58, 2861–2877.
- Clark, M.V. (2010). *Asthma: A Clinician's Guide*. Sudbury, MA : Jones & Bartlett Learning, p. 46. ISBN: 978-0763778545.
- Dettmer, S., Suhling, H., Klingenberg, I., Otten, O., Kaireit, T., Fuge, J., Kuhnigk, J.M., Gottlieb, J., Haverich, A., Welte, T., et al. (2018). Lobe-wise assessment of lung volume and density distribution in lung transplant patients and value for early detection of bronchiolitis obliterans syndrome. *eng. European Journal of Radiology* 106, 137–144.
- Fischer, B. and Modersitzki, J. (2002). Fast diffusion registration. *Contemporary Mathematics* 313, 117–128.
- Fischer, B. and Modersitzki, J. (2003). Curvature Based Image Registration. *Journal of Mathematical Imaging and Vision* 18. ID: Fischer2003, 81–85. URL: <https://doi.org/10.1023/A:1021897212261>.
- Fischer, B. and Modersitzki, J. (2008). Ill-posed medicine—an introduction to image registration. *Inverse Problems* 24, 034008. URL: <http://dx.doi.org/10.1088/0266-5611/24/3/034008>.
- Florian Jarre, J.S. (2004). *Optimierung*. Springer Berlin, Heidelberg. ISBN: 978-3-642-18785-8. DOI: <https://doi.org/10.1007/978-3-642-18785-8>.

Bibliography

- Forster, O. (2012). *Analysis 3*. 7th ed. Vieweg+Teubner Verlag Wiesbaden. ISBN:978-1-886-52914-4. DOI: <https://doi.org/10.1007/978-3-8348-2374-8>.
- Fuld, M.K., Easley, R.B., Saba, O.I., Chon, D., Reinhardt, J.M., Hoffman, E.A., and Simon, B.A. (2008). CT-measured regional specific volume change reflects regional ventilation in supine sheep. *eng. Journal of applied physiology (Bethesda, Md.: 1985)* 104, 1177–1184.
- Grob Dagmarand Oostveen, L., Rühaak, J., Heldmann, S., Mohr, B., Michielsen, K., Dorn, S., Prokop, M., Kachelrieß, M., Brink, M., and Sechopoulos, I. (2019). Accuracy of registration algorithms in subtraction CT of the lungs: A digital phantom study. *Medical Physics* 46, 2264–2274.
- Hadamard, J. (1902). Sur les Problemes Aux Derivees Partielles et Leur Signification Physique. *Princeton university bulletin*, 49–52. URL: <https://cir.nii.ac.jp/crid/1572824500616611712>.
- Horii, S.C. and Bidgood, W.D. (1993). DICOM: a standard for medical imaging. In *Enabling Technologies for High-Bandwidth Applications*, (Maitan, J., ed.). Vol. 1785. International Society for Optics and Photonics. SPIE, pp. 87–102. DOI: 10.1117/12.139249. URL: <https://doi.org/10.1117/12.139249>.
- Jorge Nocedal, S.J.W. (2006). *Numerical Optimization*. Springer New York, NY. ISBN:978-0-387-30303-1. URL: <https://doi.org/10.1007/978-0-387-40065-5>.
- Kermany, D.S., Goldbaum, M., Cai, W., Valentim, C.C.S., Liang, H., Baxter, S.L., McKeown, A., Yang, G., Wu, X., Yan, F., et al. (2018). Identifying Medical Diagnoses and Treatable Diseases by Image-Based Deep Learning. *eng. Cell* 172, 1122–1131.e9.
- Modersitzki, J. (2009). *FAIR: Flexible Algorithms for Image Registration*. *siam*.
- Murphy, K., Ginneken, B. van, Reinhardt, J.M., Kabus, S., Ding, K., Deng, X., Cao, K., Du, K., Christensen, G.E., Garcia, V., et al. (2011). Evaluation of registration methods on thoracic CT: the EMPIRE10 challenge. *eng. IEEE Transactions on Medical Imaging* 30, 1901–1920.
- North America (RSNA), R.S. of and Radiology (ACR), A.C. of (2021). *Radiation dose*. Accessed: 09.08.2022. URL: <https://www.radiologyinfo.org/en/info/safety-xray>.
- Patrick J. Lynch (2006). *Lungs diagram with internal details*. [Online; accessed May 31, 2022]. URL: https://en.wikipedia.org/wiki/Lung#/media/File:Lungs__diagram__detailed.svg.
- Ritter, F., Boskamp, T., Homeyer, A., Laue, H., Schwier, M., Link, F., and Peitgen, H.-O. (2011). *Medical Image Analysis*. *IEEE Pulse* 2, 60–70. DOI: 10.1109/MPUL.2011.942929.

Rohr, K. (2001). *Landmark-Based Image Analysis*. 1st ed. Springer Dordrecht. URL: <https://doi.org/10.1007/978-94-015-9787-6>.

Ruhaak, J., Polzin, T., Heldmann, S., Simpson, I.J.A., Handels, H., Modersitzki, J., and Heinrich, M.P. (2017). Estimation of Large Motion in Lung CT by Integrating Regularized Keypoint Correspondences into Dense Deformable Registration. *IEEE transactions on medical imaging* 36, 1746–1757. URL: <https://ieeexplore.ieee.org/document/7892934>.

Rühaak, J.R. (2017). *Matrix-free techniques for efficient image registration and their application to pulmonary image analysis*. PhD thesis. URL: <http://nbn-resolving.org/urn:nbn:de:gbv:579-opus-1007323>.

Scharm, S.C., Vogel-Claussen, J., Schaefer-Prokop, C., Dettmer, S., Knudsen, L., Jonigk, D., Fuge, J., Apel, R.-M., Welte, T., Wacker, F., et al. (2021). Quantification of dual-energy CT-derived functional parameters as potential imaging markers for progression of idiopathic pulmonary fibrosis. *European radiology* 31. ID: Scharm2021, 6640–6651. URL: <https://doi.org/10.1007/s00330-021-07798-w>.

Shin, H.-o. (2021). *METHOD FOR PROCESSING COMPUTED TOMOGRAPHY IMAGING DATA OF A SUSPECT'S RESPIRATORY SYSTEM*.

Solyanik, O., Hollmann, P., Dettmer, S., Kaireit, T., Schaefer-Prokop, C., Wacker, F., Vogel-Claussen, J., and Shin, H.-o. (2015). Quantification of Pathologic Air Trapping in Lung Transplant Patients Using CT Density Mapping: Comparison with Other CT Air Trapping Measures. *PLOS ONE* 10, e0139102. URL: <https://doi.org/10.1371/journal.pone.0139102>.

Thevenaz, P., Blu, T., and Unser, M. (2000). Image Interpolation and Resampling. In *HANDBOOK OF MEDICAL IMAGING, PROCESSING AND ANALYSIS*, Academic Press, pp. 393–420.

Winther, H.B., Gutberlet, M., Hundt, C., Kaireit, T.F., Alsady, T.M., Schmidt, B., Wacker, F., Sun, Y., Dettmer, S., Maschke, S.K., et al. (2020). Deep semantic lung segmentation for tracking potential pulmonary perfusion biomarkers in chronic obstructive pulmonary disease (COPD): The multi-ethnic study of atherosclerosis COPD study. *Journal of Magnetic Resonance Imaging* 51. <https://doi.org/10.1002/jmri.26853>; 14, 571–579. URL: <https://doi.org/10.1002/jmri.26853>.

Yushkevich, P.A., Piven, J., Hazlett, H.C., Smith, R.G., Ho, S., Gee, J.C., and Gerig, G. (2006). User-guided 3D active contour segmentation of anatomical structures: Significantly improved efficiency and reliability. *NeuroImage* 31, 1116–1128. URL: <https://www.sciencedirect.com/science/article/pii/S1053811906000632>.